

This is an Open Access document downloaded from ORCA, Cardiff University's institutional repository:<https://orca.cardiff.ac.uk/id/eprint/107182/>

This is the author's version of a work that was submitted to / accepted for publication.

Citation for final published version:

Knight, Robert, Prichard, Hazel and Ferreira Filho, Cesar F. 2017. Evidence for as contamination and the partitioning of Pd into pentlandite and Co + platinum group elements into pyrite in the Fazenda Mirabela intrusion, Brazil. *Economic Geology* 112 (8) , pp. 1889-1912. 10.5382/econgeo.2017.4533

Publishers page: <https://doi.org/10.5382/econgeo.2017.4533>

Please note:

Changes made as a result of publishing processes such as copy-editing, formatting and page numbers may not be reflected in this version. For the definitive version of this publication, please refer to the published source. You are advised to consult the publisher's version if you wish to cite this paper.

This version is being made available in accordance with publisher policies. See <http://orca.cf.ac.uk/policies.html> for usage policies. Copyright and moral rights for publications made available in ORCA are retained by the copyright holders.



# Evidence for As contamination and the partitioning of Pd into pentlandite and Co + platinum-group elements into pyrite in the Fazenda Mirabela Intrusion, Brazil.

Robert D. Knight<sup>1\*</sup>, Hazel M. Prichard<sup>1</sup>, and Cesar F. Ferreira Filho<sup>2</sup>

<sup>1</sup>School of Earth & Ocean Sciences, Cardiff University, Main Building, Park Place, Cardiff, CF10 3AT, UK

<sup>2</sup>Instituto de Geociência, Universidade de Brasília, Campus Universitário, Brasília-DF, 70910-900, Brazil

\*R.D.Knight@soton.ac.uk

\*Current address: Ocean & Earth Science, University of Southampton, Southampton, SO14 3ZH, UK

## Abstract

The Fazenda Mirabela intrusion in Brazil hosts two zones of mineralization, the Santa Rita Ni-Cu-sulfide ore zone occurring predominantly in an orthopyroxenite layer, and an underlying basal platinum-group element (PGE) anomaly hosted in S-poor dunite. We show that in the northern and southern (marginal) zones of the intrusion, (Pt,Pd,Ni,Cu)(Fe,Bi,Te)<sub>2</sub> minerals are accompanied by As-bearing platinum group minerals (PGM) sperrylite (PtAs<sub>2</sub>), and irarsite ([RhIrPt]AsS). These As-bearing PGM are extremely rare in the central zone of the intrusion, suggesting that As has been introduced into the margins of the intrusion from the country rocks via crustal assimilation or syn-magmatic hydrothermal processes. Other PGM and precious metal minerals (PMM) including hessite (Ag<sub>2</sub>Te), Pd-Ag tellurides, electrum, and native Au are observed in the Santa Rita ore zone and do not show any lateral variation. In the semimetal-poor, S-poor dunite hosting the basal PGE anomaly, PGE are predominantly retained in the base metal sulfides and only minor PGE alloys are present. In this S-poor dunite Pt, Au and semimetals partitioned into a fractionated Cu-rich liquid which formed during the crystallization of monosulfide solid solution (MSS) and was largely removed by high temperature magmatic fluids. Palladium was not affected by this process and significant concentrations of Pd are identified in pentlandite, suggesting that Pd preferentially partitioned into MSS as it crystallized and subsequently pentlandite as it exsolved. Pyrite in the Santa Rita ore zone is Co-rich and contains higher concentrations of IPGE (Os, Ir, Ru) and Rh than pyrrhotite and pentlandite, suggesting that pyrite has not replaced and inherited the PGE concentrations of these sulfides. The Pd-poor nature of pyrite also indicates that it has not replaced Pd-rich pentlandite. It is proposed that the IPGE and Co preferentially partitioned into pyrite as it exsolved from MSS.

Keywords: Fazenda Mirabela, Platinum-group elements, Sulfide, Pyrite, Arsenic

## Introduction

The Fazenda Mirabela ultramafic-mafic layered intrusion located in Bahia State, north-eastern Brazil (Fig. 1), hosts the stratiform Santa Rita Ni-Cu-sulfide ore zone (Barnes et al., 2011; Inwood et al., 2011). This ore zone varies in thickness up to 200 m and is

40 situated within the upper part of the ultramafic sequence, close to the boundary with the  
41 mafic sequence, and hosts appreciable concentrations of platinum-group elements (PGE) with  
42 Pt + Pd typically between 0.1–0.5 ppm. A second zone of sulfur-poor PGE mineralization  
43 underlies the Santa Rita ore zone and is referred to herein as the ‘basal PGE anomaly’  
44 following the nomenclature of Barnes et al. (2011).

45 The Santa Rita ore zone has extremely high Ni tenors while remaining relatively  
46 PGE-poor. The formation of this deposit and its Ni-rich nature has been attributed to the  
47 prolonged mixing of an initially magnesian, moderately Ni-enriched resident “M-type  
48 magma” close to sulfide saturation, with a relatively Ni-PGE-depleted and cooler  
49 replenishing “G-type magma” charged with suspended sulfide liquid droplets (Barnes et al.,  
50 2011). A contributing factor in forming high Ni tenors may be the reaction between the  
51 sulfide liquid and coexisting olivine in an environment where both phases equilibrate with a  
52 large reservoir of silicate magma; furthermore, higher Ni content in the sulfide liquid gives  
53 rise to an increased tendency for Ni to partition into sulfide from adjacent olivine, forming a  
54 positive feedback mechanism (Barnes et al., 2011).

55 The Fazenda Mirabela intrusion has been divided into three zones for mining  
56 purposes; central, southern, and northern (Fig. 2). The platinum-group mineralogy of 21  
57 samples from two boreholes in the central zone of the intrusion has been documented by  
58 Knight et al. (2011). They identified Pt-Pd-Ni tellurides accompanied by Ag tellurides, minor  
59 electrum, and native Au in the both the Santa Rita ore zone and the underlying basal PGE  
60 anomaly, however, they also recognized a localized PGE alloy assemblage dominated by Pd-  
61 Cu alloys in samples from the basal PGE anomaly in one borehole. Here we build on this  
62 study by documenting the platinum-group minerals (PGM) and precious metal minerals  
63 (PMM) in samples from four new boreholes; two from the northern zone and two from the  
64 southern zone of the intrusion. Laser ablation (LA)-ICP-MS and whole-rock geochemical  
65 analyses have been completed on samples from the northern and southern zones as well as  
66 those from the central zone studied by Knight et al. (2011). These combined data fully  
67 characterize the PGE mineralization in the Fazenda Mirabela intrusion and are used to  
68 explain some unusual features of the Santa Rita ore zone and the underlying basal PGE  
69 anomaly.

70

71

## **Regional and Local Geology**

### *Regional geology*

73 The Fazenda Mirabela intrusion is part of a cluster of ultramafic-mafic complexes  
74 located in the southern portion of the Paleoproterozoic Itabuna-Salvador-Curaça belt. The  
75 latter comprises a low-K calc-alkaline plutonic suite formed during the collision of Archean  
76 blocks during the ~2.15–2.05 Ga Transamazonian orogeny (Barbosa and Sabaté, 2004). The  
77 immediate country rocks to the intrusion are comprised of a supracrustal sequence of gneisses  
78 and minor metamorphosed banded iron formations, metabasic sills, as well as a deformed  
79 sequence of granulite facies charnockite and enderbite orthogneisses (Fig. 1; Barbosa et al.,  
80 2003). The intrusion of the largely unaltered and undeformed Fazenda Mirabela and Palestina  
81 igneous bodies (~2065 Ma; Ferreira Filho et al., 2013) postdates the regional granulite facies  
82 metamorphism of the country rocks (2086 ± 7 Ma; Peucat et al., 2011).

83

#### 84 *Stratigraphy of the Fazenda Mirabela intrusion*

85           The north-easterly dipping Fazenda Mirabela intrusion covers a surface area of ~7  
86 km<sup>2</sup> and consists primarily of a lower ultramafic sequence exposed to the west and an upper  
87 mafic sequence exposed to the east (Fig. 2). Individual layers become progressively thinner  
88 towards the southern and northern borders (Ferreira Filho et al., 2013). The stratigraphic base  
89 of the Fazenda Mirabela intrusion is a reversely differentiated sequence comprising ~90 m of  
90 gabbro-norite overlain by ~150 m of orthopyroxenite. These units are overlain by the  
91 ultramafic sequence (~750 m thick), consisting of ~600 m of dunite followed by a ~150 m  
92 sequence of harzburgite, olivine orthopyroxenite, and orthopyroxenite that is capped by a thin  
93 1-2 m websterite unit. The thickness of individual layers in the upper portion of the  
94 ultramafic sequence is variable and characterized by interlayered rock types (Ferreira Filho et  
95 al., 2013). This is overlain by the mafic sequence (~1300 m thick) comprised of monotonous  
96 gabbro-norite. The intrusion shows no evidence of the high-grade metamorphism and  
97 deformation that has affected the surrounding country rocks, but has been cross-cut by late  
98 minor dolerite and felsic pegmatitic dykes. Significant laterization has occurred at the surface  
99 of the intrusion, particularly over the lower (or western) ultramafic sequence (Inwood et al.,  
100 2011).

101

#### 102 *Mineralization*

103           The Santa Rita Ni-Cu-(PGE) sulfide orebody is a semi-continuous stratabound zone  
104 of disseminated sulfides situated within the upper ~100 m of the ultramafic sequence,  
105 predominantly in the orthopyroxenite unit (excluding the uppermost part of this lithology),  
106 extending down into the upper part of the harzburgite (Barnes et al., 2011). The orebody  
107 varies in thickness and in its exact position within the igneous stratigraphy from the north to  
108 the south of the intrusion. The ore zone occurs as a single well-defined layer ~50 m thick in  
109 the northern part of the intrusion and transitions into a thick (up to ~200 m) discontinuous  
110 zone at the southern margin of the intrusion while transgressing upwards through the  
111 ultramafic stratigraphy (Barnes et al., 2011). The ore zone typically consists of 0.5-3.0 vol. %  
112 disseminated sulfides, and is PGE bearing with Pt + Pd concentrations typically between 0.1-  
113 0.5 ppm (Fig. 3). The base metal sulfide (BMS) assemblage is dominated by pentlandite  
114 (~50%) which is accompanied by variable but progressively lesser amounts of pyrite,  
115 pyrrhotite, and chalcopyrite. The combined proven and probable reserves of the Santa Rita  
116 deposit as of 31 December 2010 stood at 159 million metric tons at 0.52 wt. % Ni, 0.13 wt. %  
117 Cu, 0.015 wt. % Co, and 86 ppb Pt (Mirabela Nickel Ltd., Annual Report, 2011).

118           Primary magmatic minerals and textures are well preserved (Fig. 4). Two main types  
119 of sulfide morphology are observed: i) BMS occurring interstitially to olivine and  
120 orthopyroxene crystals (Fig. 4A-B), and ii) small fine grained sulfides which are intergrown  
121 with fine grained intercumulus silicate phases (plagioclase, clinopyroxene and phlogopite).  
122 Interstitial sulfides exhibit low dihedral angles, but more commonly have rounded  
123 terminations that were previously noted by Barnes et al. (2011) who also described the  
124 silicate mineralogy and chemistry in greater detail. Interstitial sulfide blebs (typically ~1 mm  
125 across) consist of cores of pentlandite, usually intergrown with euhedral pyrite (Fig. 4C),

126 partially surrounded by chalcopyrite and pyrrhotite. Minor BMS are also observed within the  
127 separated cleavage planes of orthopyroxene crystals.

128 Sulfide stringers composed of pentlandite, pyrrhotite, and chalcopyrite are observed  
129 extending from interstitial sulfides. These are often only a few microns wide and are  
130 commonly aligned, giving rise to a pseudo-fabric within the rock. Minor localized patches  
131 and veins of post-magmatic serpentinisation are observed in the Santa Rita ore zone and in  
132 some cases these are associated with the BMS stringers.

133 A zone of S-poor (<0.1 wt. % S) PGE mineralization forming the basal PGE anomaly  
134 is observed in the upper part of the dunite, underlying the Santa Rita ore zone (Fig. 3). This  
135 dunite displays a decoupling of S and PGE, with Pt and Pd tenors for this zone calculated to  
136 be significantly higher (~20 ppm for both Pt and Pd) than those of the relatively BMS-rich  
137 Santa Rita ore zone (Barnes et al., 2011). The basal PGE anomaly typically occurs between  
138 50-75 m below the base of the Santa Rita ore zone and is observed in the central zone and  
139 southern zone boreholes; the depth of the northern zone boreholes is not sufficient to intersect  
140 this anomaly. The sulfides are finely disseminated forming small (< 150 µm across)  
141 interstitial crystals dominated by pentlandite accompanied by minor chalcopyrite, with  
142 pyrrhotite and pyrite virtually absent (Fig. 4D). Micro-scale sulfide-silicate graphic textures  
143 that resemble symplectites are commonly observed (Fig. 4E-F) and are often associated with  
144 phlogopite.

145

146

### **Sampling and Analytical Methods**

147 Drill core from four boreholes was sampled; two from the northern zone (MBS209  
148 and MBS158; samples PTRS26-49) and two from the southern zone (MBS565 and MBS569;  
149 samples PTRS50-72). Borehole locations and additional information are given in Figure 2  
150 and Table 1, respectively. Sampling was completed with the aid of mine assay data to  
151 identify samples with the highest PGE contents and was extended ~100 m above and below  
152 the defined economic limits of the Santa Rita ore zone in order to sample all lithologies  
153 present in the intrusion, and the basal PGE anomaly where intersected.

154 A total of 47 samples were collected; 12 from each borehole sampled, except for  
155 MBS565 where only 11 samples were taken as a sample of gabbronorite could not be  
156 obtained from this hole. The silicate and sulfide mineralogy of all samples were characterized  
157 using transmitted and reflected light microscopy of polished thin sections. Detailed analysis  
158 of the platinum-group mineralogy was conducted on 40 samples; gabbronorite and websterite  
159 samples were not studied given their low PGE concentrations. Platinum-group and precious  
160 metal minerals and their associated sulfide, silicate, and oxide minerals were identified and  
161 analyzed using a Cambridge Instruments (now Carl Zeiss NTS) S360 scanning electron  
162 microscope (SEM). Polished thin sections were searched systematically for PGM using the  
163 SEM set at a magnification of 100x. Quantitative analyses of the larger PGM (> 0.3 x 0.3  
164 µm) were obtained using an Oxford Instruments INCA Energy EDX analyzer attached to the  
165 SEM. Operating conditions for the quantitative analyses were 20 kV, with a specimen  
166 calibration current of ~1 nA and a working distance of 25 mm. A cobalt reference standard  
167 was regularly analyzed in order to check for any drift in the analytical conditions. A  
168 comprehensive set of standards obtained from MicroAnalysis Consultants Ltd. (St Ives,

169 Cambridgeshire) were used to calibrate the EDX analyzer. Semi-quantitative analyses of  
170 smaller PGM ( $< 0.3 \times 0.3 \mu\text{m}$ ) were determined by accounting for elements derived from the  
171 host minerals. Images were obtained using a four-quadrant back-scattered detector operating  
172 at 20 kV, a beam current of  $\sim 500 \text{ pA}$ , and a working distance of 13 mm, under which  
173 conditions, magnifications of up to 15000x are possible.

174 Commercial mine assay data were obtained from one meter composite intervals of  
175 diamond drill core by ALS Chemex Ltd., Vancouver, Canada. Fire assay was used to  
176 determine Au, Pt, and Pd by ICP-MS finish while multi-element ICP-MS was used to obtain  
177 data for the other elements reported here.

178 Whole-rock PGE (excluding Os) and Au data were determined by Actlabs via Ni-fire  
179 assay for all samples from the northern and southern zones (PTSR26-72) as well as samples  
180 from the central zone (PTSR01-25 from boreholes MBS604 and MBS605; Fig. 2) studied by  
181 Knight et al. (2011). Semimetal concentrations (As, Bi, Sb, Te) were determined by aqua  
182 regia digest and ICP-MS finish by Actlabs for samples PTSR26-72 from the northern and  
183 southern zones of the intrusion.

184 A selection of 31 samples from all six boreholes studied (central, northern and  
185 southern zones) from both the Santa Rita ore zone and the underlying basal PGE anomaly  
186 were analyzed using LA-ICP-MS at Cardiff University. This was carried out using a New  
187 Wave Research UP213 UV laser system coupled to a Thermo X Series 2 ICP-MS. Platinum-  
188 group elements and other elements were determined in time-resolved analysis mode (time  
189 slices of 350 ms) as the laser beam followed a line designed to sample different sulfide  
190 phases. The beam diameter employed was  $30 \mu\text{m}$ , with a frequency of 10 Hz, and the sample  
191 was translated at  $6 \mu\text{m/s}$  relative to the laser. Acquisitions lasted between 80-400 s, and a gas  
192 blank was measured for 30-40 s prior to analysis. The internal standard used was  $^{33}\text{S}$  and this  
193 was measured for the analyzed sulfides quantitatively using the SEM. Subtraction of gas  
194 blanks and internal standard corrections were performed using Thermo PlasmaLab software.

195 In order to show that these analyses represent PGE in solid solution, laser traces that  
196 indicated higher than average Te or As concentrations coupled with anomalously high PGE  
197 have been discounted from the data set as it is likely that PGM (predominantly Te- or As-  
198 bearing PGM) were intercepted in these cases. Similarly, analyses have also been discounted  
199 where the time resolved spectra have clearly indicated the presence of PGM or PGM micro-  
200 inclusions.

201 Calibration was performed using five synthetic Ni-Fe-S standards prepared from  
202 quenched sulfides. The standards incorporate S, Ni, Fe, and Cu as major elements and Co,  
203 Zn, As, Se, Ru, Rh, Pd, Ag, Cd, Sb, Te, Re, Os, Ir, Pt, Au, and Bi as trace elements. The  
204 compositions of these sulfide standards are given in Prichard et al. (2013). The standards  
205 produce five point calibration curves for S, Ni, and Fe. Standards 1, 4, and 5 produce three  
206 point calibration curves for the PGE, Ag, Cd, Re, Au, and semimetals. Standards 1-3 produce  
207 three point calibration curves for Cu, Co, and Zn, and reliable matrix-matched corrections for  
208 argide species ( $^{59}\text{Co}^{40}\text{Ar}$ ,  $^{61}\text{Ni}^{40}\text{Ar}$ ,  $^{63}\text{Cu}^{40}\text{Ar}$ ,  $^{65}\text{Cu}^{40}\text{Ar}$ ,  $^{66}\text{Zn}^{40}\text{Ar}$ ) that interfere with light  
209 PGE isotopes. Corrections for  $^{106}\text{Cd}$  on  $^{106}\text{Pd}$  and  $^{108}\text{Cd}$  on  $^{108}\text{Pd}$  were determined using  
210 Standard 1. Where independent corrections have been applied to different isotopes of the  
211 same element (e.g.,  $^{66}\text{Zn}^{40}\text{Ar}$  on  $^{106}\text{Pd}$  and  $^{108}\text{Cd}$  on  $^{108}\text{Pd}$ ) the independently corrected values  
212 vary by  $<20\%$  (and commonly  $<5\%$ ) indicating that these corrections are robust. The

213 accuracy of the LA-ICP-MS procedure for PGE was checked by the analysis of the  
214 Laflamme-Po724 standard run as an unknown against the Cardiff sulfide standards at the start  
215 and end of each day.

216

## 217 **Results**

### 218 *Whole-rock PGE and semimetal concentrations*

219 Three distinct patterns are shown in the Fazenda Mirabela whole-rock PGE data  
220 plotted as chondrite normalized profiles, using the values given in Lodders (2003). They all  
221 have positive trends but exhibit variations in Pd, Pt, and Au concentrations. Pattern A is  
222 defined by negative Pd anomalies and is typically observed in orthopyroxenite, olivine  
223 orthopyroxenite, and harzburgite samples from the Santa Rita ore zone. Pattern B is defined  
224 by positive slopes without any significant anomalies and occurs primarily in harzburgite  
225 samples in the transition zone between the Santa Rita ore zone and the underlying basal PGE  
226 anomaly. Pattern C is defined by positive Pd and negative Au (and Pt) anomalies and  
227 typically occurs in samples from the basal PGE anomaly in the S-poor dunite. It is not  
228 feasible to show all whole-rock PGE patterns for every sample analyzed, so an example is  
229 given using the samples from borehole MBS569 in the southern zone in conjunction with a  
230 stratigraphic section showing the locations of the samples and where these different PGE  
231 patterns occur in the Fazenda Mirabela stratigraphy (Fig. 5).

232 Data from the central and southern zone boreholes is shown graphically using two  
233 plots of Pt/Pd versus Pd/Ru and Au/Pd versus Pd/Ru (Fig. 6); northern zone boreholes have  
234 been omitted as the stratigraphy is slightly more complex. These plots demonstrate that S-  
235 poor dunite samples from the basal PGE anomaly have low Pt/Pd and Au/Pd ratios, whereas  
236 samples above this zone, including the Santa Rita ore zone, have high Pt/Pd and Au/Pd ratios.

237 Whole-rock semimetal concentrations (As, Bi, Sb, and Te) for all samples studied  
238 from southern boreholes MBS565 and MBS569 (Table 2) reveal that Bi and Sb  
239 concentrations are very low and considered insignificant in the majority of samples studied.  
240 However, meaningful As and Te concentrations are noted and these correlate closely with S  
241 (Fig. 7). An understanding of the distribution of the whole rock concentrations of these  
242 semimetals throughout the intrusion is important as they control the PGE mineralogy.

243

### 244 *Platinum-group and precious metal mineralogy*

245 More than 500 platinum-group and precious metal minerals have been documented in  
246 the northern and southern zones of the Fazenda Mirabela intrusion (Table 3) and quantitative  
247 analyses of these PGM have been undertaken where possible (Table 4). A further 217 PGM  
248 and PMM were identified in the central zone of the intrusion (Knight et al., 2011). Three  
249 distinct PGM assemblages are observed in the Fazenda Mirabela intrusion which are  
250 described below. The location of all three PGM assemblages is provided in Figure 8.

251

252 Marginal assemblage

253 The marginal PGM assemblage is observed in the northern and southern zones of the  
254 intrusion and consists of (Pt,Pd,Ni,Cu)(Fe,Bi,Te)<sub>2</sub> minerals and As-bearing PGM,  
255 predominately sperrylite (PtAs<sub>2</sub>) and members of the hollingworthite-irarsite-platarsite solid  
256 solution series ([RhIrPt]AsS). Minor Ag-Pd-Te minerals, electrum ± Fe-Cu, and native Au  
257 grains are observed, with accessory hessite (Ag<sub>2</sub>Te) common.

258 Throughout the Santa Rita ore zone, the BMS occur interstitially to the silicates (Fig.  
259 4A-B) with stringers composed of pentlandite, pyrrhotite, and chalcopyrite that extend from  
260 the interstitial BMS into the silicates along grain boundaries and occasionally along separated  
261 cleavage planes in orthopyroxene. Platinum-group minerals occur within BMS, on their  
262 margins, and in BMS stringers. The BMS stringers host both PGE-bearing tellurides (Fig. 9E-  
263 F) and sperrylite (Fig. 10D-E). These stringers connect to interstitial composite sulfides and  
264 PGM are observed both proximally (Fig. 9F and 10D) and distally (Fig. 9E and 10E) to the  
265 interstitial sulfides. The stringers are roughly aligned producing a pseudo-fabric in the rock  
266 and may be enclosed by serpentine in some occurrences (Fig. 9E).

267 Despite the presence of arsenides, the most common PGM (n=322) identified in the  
268 marginal assemblage belong to the (Pt,Pd,Ni)(Fe,Bi,Te)<sub>2</sub> solid solution series (Table 3) and  
269 vary in size from 0.5-639.6 μm<sup>2</sup> (avg. 30.1 μm<sup>2</sup>). In the absence of Fe and Bi, these PGM are  
270 merenskyite (PdTe<sub>2</sub>), moncheite, (PtTe<sub>2</sub>), and melonite (NiTe<sub>2</sub>). The proportions of Pt:Pd:Ni  
271 in these PGM have been plotted on a ternary diagram using semi-quantitative atomic weight  
272 data collected using the SEM (Fig. 11). This plot shows the abundance of Ni-dominant PGM  
273 which is in keeping with the high Ni content of the system as demonstrated by the proportion  
274 of pentlandite to other sulfide phases. These PGE-bearing tellurides are typically rounded  
275 (Fig. 9A-B) or lath shaped (Fig. 9C-D) with the majority associated with BMS (Fig. 13).  
276 These PGM are observed enclosed by a single sulfide phase (Fig. 9A-B), crossing sulfide  
277 phase boundaries (Fig. 9C), and as laths at the edge of BMS and in contact with adjacent  
278 silicates (Fig. 9D). In contrast to the central zone, Cu-bearing tellurides are observed (CuTe)  
279 and Cu also substitutes for Pt, Pd, and Ni in some PGM (Table 4).

280 The major difference in the platinum-group mineralogy between the margins of the  
281 intrusion and the central zone is the significant increase in As-bearing PGM observed at the  
282 margins. Sperrylite crystals are relatively abundant, with 69 identified in the northern and  
283 southern zones compared to four in the central zone. They typically range in size between  
284 0.8-463.3 μm<sup>2</sup> with smaller crystals occurring more regularly. The largest sperrylite  
285 identified falls outside of this range and is ~1.5 mm<sup>2</sup>. Sperrylite is commonly situated within,  
286 or closely associated with the BMS (Fig. 10A-D) with only 20% of identified grains observed  
287 wholly within silicate or oxide phases. These PGM are euhedral with tabular forms when not  
288 hindered by the host sulfide.

289 Platinum-group minerals that belong to the hollingworthite-irarsite-platarsite solid  
290 solution series ([RhIrPt]AsS) have also been identified (Fig. 10F); 18 in the northern and  
291 southern zones compared to three in the central zone. Ten are Ir-dominant, all of which are  
292 Pt-bearing. Five are Pt-dominant, four of which are Ir-bearing, and one is Rh-bearing. The  
293 remaining three are Rh-dominant and are slightly more complex with the addition of Os (Rh-  
294 Ir-Pt-As-S, Rh-Pt-Os-As-S, Rh-Pt-Os-Ir-As-S). The size range of these PGM is relatively  
295 small, between 0.6-7.7 μm<sup>2</sup>, with only one crystal larger than this range identified at 14.4  
296 μm<sup>2</sup>. The majority of these PGM (85%) are located at the edge of, or within BMS (Fig. 10F),

297 with only four identified in silicates; two of which retain a close association with sulfides  
298 (Fig. 13).

299 Two types of silver tellurides are observed, hessite which is common, and rarer Ag-  
300 Pd-Te. Hessite crystals range in size from 0.3-248.9  $\mu\text{m}^2$  (avg. 16.2  $\mu\text{m}^2$ ). These tellurides are  
301 typically subhedral-anhedral with a minority exhibiting lath crystal forms. They are  
302 predominantly observed within BMS (Fig. 12A-B) and rarely in silicates. The Ag-Pd-Te  
303 crystals exhibit the same behavior and crystal forms as hessite, however, they are less  
304 common and smaller, between 0.7-17.5  $\mu\text{m}^2$  (avg. 5.3  $\mu\text{m}^2$ ).

305 Several different types of Au-bearing alloys have been identified which are  
306 commonly associated with BMS and consist of electrum, Au-Cu, Au-Ag-(Cu-Fe) (Fig. 12C),  
307 and native Au (Fig. 12D). These Au-bearing alloys are typically anhedral and the majority  
308 range in size between 0.4-126.7  $\mu\text{m}^2$  (avg. 13.6  $\mu\text{m}^2$ ).

309 Five Pt-S minerals have been identified which are extremely variable in size between  
310 ~4-110  $\mu\text{m}^2$ . They exhibit subhedral-euhedral crystal forms including three which are lath  
311 shaped. Three are situated within BMS while the remaining two are found in a silicate and  
312 oxide phase, respectively. Rare PGE-bearing alloys have also been identified which include  
313 one of each of the following; Pd-Cu, Ru-Os, Pt-Fe, and Pt-Ir. These PGE alloys are relatively  
314 small (<6  $\mu\text{m}^2$ ) and are all located within BMS.

315

#### 316 Central zone assemblage

317 The central zone assemblage contains predominantly (Pt,Pd,Ni)(Fe,Bi,Te)<sub>2</sub>  
318 accompanied by accessory hessite (Ag<sub>2</sub>Te), rare electrum and native Au grains observed in  
319 both the Santa Rita ore zone and the basal PGE anomaly in the underlying S-poor dunite in  
320 one borehole only (MBS605) (Knight et al., 2011). Platinum-group and precious metal  
321 mineral sizes, textures, and mineral associations are identical to the same minerals described  
322 in the marginal zones above. The main difference in PGM between the central zone and the  
323 northern and southern zones of the intrusion is the almost complete absence of As-bearing  
324 PGM in the central zone.

325

#### 326 Localized PGE alloy assemblage

327 In the basal PGE anomaly hosted in the S-poor dunite and underlying the Santa Rita  
328 ore zone, a localized PGE alloy assemblage is observed only in one borehole (MBS604) in  
329 the central zone. This assemblage comprises predominately Pd-Cu-(Pb) alloys (Fig. 12E-F)  
330 accompanied by minor PGE-bearing arsenides (Knight et al., 2011). The PGM are associated  
331 with pentlandite and chalcopyrite, effectively the only two sulfide phases present in the S-  
332 poor dunite zone. PGM exhibit subhedral-euhedral forms where they are associated with  
333 unaltered fresh magmatic sulfides as in the Santa Rita ore zone. However, PGM are also  
334 associated with BMS exhibiting micro-scale sulfide-silicate graphic textures resembling  
335 symplectites, and in these cases the PGM are typically situated at the crystal edges and  
336 exhibit anhedral crystal forms (Fig. 12E-F).

337

338 PGM abundance and size distribution

339 The difference in mineralogy between the central zone (excluding the Pd-Cu alloy  
340 assemblage) and the margins of the intrusion are illustrated by pie charts based on both the  
341 number of each PGM and PMM type identified, and the combined surface area each PGM  
342 and PMM type identified (Fig. 14A-D); the Pd-Cu alloy assemblage is plotted separately  
343 (Fig. 14E-F). These plots demonstrate the significant variation in As-bearing PGM across the  
344 intrusion and the dominance of PGE alloys in the localized Pd-Cu alloy assemblage.

345 The abundance and size of PGM and PMM identified in the Fazenda Mirabela  
346 intrusion, including data from the central zone of the intrusion, varies between the Santa Rita  
347 ore zone and the underlying basal PGE anomaly in the S-poor dunite, regardless of which  
348 PGM assemblage is present. In the Santa Rita ore zone, PGM and PMM are larger, typically  
349 ranging between 1-24.9  $\mu\text{m}^2$  and are more abundant with ~17 PGM and PMM identified per  
350 sample (thin section) studied (Fig. 15). In the underlying S-poor dunite, the PGM and PMM  
351 are smaller, with >80% of those identified < 8.9  $\mu\text{m}^2$ . They are also much less abundant with  
352 only ~5 PGM and PMM identified per sample (thin section) studied (Fig. 15).

353

354 *Laser ablation-ICP-MS*

355 Laser ablation analyses of the sulfides show the presence of PGE-poor BMS in the  
356 Santa Rita ore zone, and PGE-rich BMS in the basal PGE anomaly in the S-poor dunite  
357 (Table 5; Fig. 16).

358

359 Santa Rita ore zone

360 In the Santa Rita ore zone, the BMS host very low concentrations of PGE in solid  
361 solution. In both chalcopyrite and pyrrhotite, the average concentrations of all six PGE  
362 individually are <1 ppm. The highest Rh and Pt concentrations recorded in any sulfide phase  
363 are 1.1 ppm (pentlandite) and 1.6 ppm (pyrrhotite), respectively. Osmium concentrations can  
364 be relatively high (up to 4.5 ppm), however, these values are rare as evidenced by a low  
365 average value of <1 ppm. Pentlandite is the principal host of the PGE, with Pd concentrations  
366 of up to 13 ppm and an average value of 2.3 ppm; pentlandite also hosts low but significant  
367 average concentrations of Os (0.52 ppm) and Ru (0.91 ppm). More unusual is the  
368 identification of Os, Ir, Ru, and Rh in pyrite (Fig. 16A), with concentrations of up to 2.2 ppm  
369 Os, 1.0 ppm Ir, 3.7 ppm Ru, and 0.8 ppm Rh recorded, and average values of 0.6 ppm, 0.2  
370 ppm, 0.8 ppm, and 0.1, respectively. Furthermore, pyrite also consistently hosts significant  
371 concentrations of cobalt, between 0.8-3.2 wt. %. Time resolved spectra show that  
372 concentrations of these PGE and Co in pyrite are not the result of intersecting discrete PGM  
373 or other mineral phases (Fig. 17A).

374

375 Basal PGE anomaly

376 The BMS analyzed from the S-poor dunite host very high concentrations of PGE.  
377 Pentlandite is the most PGE-enriched sulfide in these samples hosting high average  
378 concentrations of all six PGE (Fig. 16B); 4.2 ppm Os, 1.7 ppm Ir, 6.3 ppm Ru, 4.3 ppm Rh,

379 4.3 ppm Pt, and 42.5 ppm Pd. The highest concentrations identified are as follows; 38.3 ppm  
380 Os, 28.7 ppm Ir, 59.1 ppm Ru, 36.1 ppm Rh, 254 ppm Pd, and 28.9 ppm Pt. Time resolved  
381 spectra show that high concentrations of Pd, Ir, and particularly Pt in pentlandite are not the  
382 result of intersecting discrete PGM or other mineral phases (Fig. 17B).

383 In the basal PGE anomaly, chalcopyrite is the least PGE enriched sulfide and contains  
384 low average concentrations (<1 ppm) of Os, Ir, Ru, Rh, and Pt, but significant average  
385 concentrations of Pd (8.8 ppm). One of two pyrite crystals analyzed contains significant  
386 concentrations of IPGE (6 ppm Os, 2.5 ppm Ir, and 5.6 ppm Ru) while being poor in Rh, Pt,  
387 and Pd, however, the second pyrite crystal analyzed is generally PGE-poor with individual  
388 PGE concentrations all <1 ppm. These results are not statistically significant as only three  
389 chalcopyrite crystals and two pyrite crystals were analyzed due to the small size and rarity of  
390 these phases, respectively.

391 In many cases, quantitative analyses of individual sulfide phases could not be  
392 completed in this zone due to the small size of the sulfides and the resulting overlap of  
393 signals from adjacent silicates and oxides. Where interstitial sulfides were ablated, the signals  
394 of more than one sulfide phase often overlapped and could not be distinguished from one  
395 another to allow for the quantification of PGE in each individual phase. Therefore, average  
396 PGE concentrations were determined from the combination of two or three sulfide phases  
397 where signals from silicate and oxides minerals were absent. In these cases, the analyses are  
398 reported as BMS mixtures, most commonly a mixture of pentlandite and chalcopyrite (e.g.,  
399 Pn-Cpy; Table 5). These composite sulfide analyses have been ignored in the Santa Rita ore  
400 zone for clarity, where all sulfide phases are large and relatively common, but have been  
401 included for the S-poor dunite samples given their significant PGE content and the rarity of  
402 relatively large mono-phase sulfides in this zone.

403 Average concentrations of PGE in pentlandite-chalcopyrite BMS mixtures are  
404 relatively high at 1.2 ppm Os, 3.3 ppm Ru, 2.2 ppm Rh, 2.6 ppm Pt and 42.4 ppm Pd, with  
405 ranges given in Table 5. However, these sulfides are Ir-poor with an average concentration of  
406 only 0.6 ppm. The highest Pd concentrations identified overall are 371 ppm and 570 ppm  
407 occurring in two other BMS mixtures consisting of pentlandite-pyrite and pentlandite-pyrite-  
408 chalcopyrite, respectively.

409

410

## Discussion

411 This investigation into the PGE mineralization in the Fazenda Mirabela intrusion has  
412 revealed several interesting results that require discussion. These include: the variation from  
413 predominately PGE tellurides in the central zone to a combination of PGE-bearing tellurides  
414 and arsenides in the northern and southern zones (margins) of the intrusion, as well the  
415 overall genesis of these PGM; the formation of BMS stringers and their associated PGM; the  
416 formation of high PGE tenor sulfides in a system with relatively low PGE concentrations; and  
417 the origin of significant IPGE, Rh, and high Co concentrations in pyrite.

418

419 *Formation of Te- and As-bearing PGM*

420 The PGE-bearing tellurides are typically rounded and lath shaped, and probably  
421 formed via the exsolution of Pt, Pd, Ni, and Te from BMS (Knight et al., 2011) as suggested  
422 for these minerals both experimentally (Peregoedova et al., 2004) and naturally during the  
423 slow cooling intrusions (Barnes et al., 2008). Alternatively, Knight et al. (2011) suggested  
424 that these PGM crystallized directly from a late stage fractionated semimetal-rich liquid into  
425 which Pt, Pd, and excess Ni were concentrated during the crystallization of monosulfide solid  
426 solution (MSS) and intermediate solid solution (ISS). This suggestion is based on the  
427 incompatibility of these PGE with MSS (e.g., Fleet et al., 1993; Li et al., 1996; Ballhaus et  
428 al., 2001; Mungall et al., 2005) and ISS (Peregoedova, 1998), particularly in the presence of  
429 semimetals, specifically Te (Helmy et al., 2007; Holwell and McDonald, 2007; Hutchinson  
430 and McDonald, 2008; Helmy et al., 2010).

431 The timing of formation of the As-bearing PGM (sperrylite and members of the  
432 hollingworthite-irarsite-platarsite solid solution series) in the Santa Rita marginal ore zone  
433 deserves consideration (Fig. 8 and 10). These types of As-bearing PGM when observed  
434 completely enclosed by silicates and oxides are often interpreted to have crystallized early,  
435 directly from an immiscible sulfide melt and are then trapped in these later crystallizing  
436 phases (e.g., Coghill and Wilson, 1993; Hutchinson and McDonald, 2008; McDonald, 2008;  
437 Dare et al., 2010a). However, these PGM may maintain an association with BMS if, for  
438 instance, they do not cleanly separate from the sulfide liquid from which they have  
439 crystallized. This may have occurred in the Fazenda Mirabela intrusion where the majority of  
440 these PGM remain associated with BMS (Fig. 10A-D) and could explain why some sperrylite  
441 crystals are much larger than their host sulfides. In these cases, exsolution of PGE from the  
442 small BMS host could not account for PGM formation (Fig. 10C). It should be noted,  
443 however, that the observation of PGM larger than their host sulfide is two-dimensional and  
444 potentially not reliable. Sperrylite, where observed in primary magmatic BMS stringers, may  
445 have formed via exsolution from the sulfides during cooling; it is unlikely that they  
446 crystallized early in stringer form before the crystallization of the silicates (Fig. 10D-E).

447 The spatial variation in sperrylite and irarsite across the intrusion whereby these As-  
448 bearing PGM are restricted to the northern and southern margins may be explained by the  
449 possible addition of As from the surrounding country rocks via crustal assimilation. Crustal  
450 assimilation is a widely accepted process by which sulfide saturation can be achieved in  
451 ultramafic-mafic systems evidenced by: non-mantle sulfur isotopes ratios (e.g., Noril'sk and  
452 Duluth; Ripley, 1981; Ripley and Aljassar, 1987; Li et al., 2003); the association of magmatic  
453 sulfides with xenoliths (e.g., Voisey's Bay and Duluth; Ripley and Alawi, 1986; Mariga et  
454 al., 2006); and the association of sulfide ores with evaporites (e.g., Noril'sk ; Naldrett et al.,  
455 1992). Recently, this process has been examined in detail at Duluth by Samalens et al.  
456 (2017), who found that the contamination of the mafic magma by both sulfur and the  
457 semimetals results from the transfer of sulfide droplets from country rock xenoliths in a  
458 mobile, silicate partial melt.

459 Increased As concentrations have been linked to the local assimilation of country rocks  
460 (Ames and Farrow, 2007), and crustal assimilation is thought to be responsible for the  
461 localized crystallization of As-bearing PGM in both the Creighton deposit, Sudbury (Dare et  
462 al., 2010a), and the Platreef in the Bushveld Complex (Hutchinson and McDonald, 2008).  
463 The distribution of As-bearing PGM in the Fazenda Mirabela intrusion is also localized and  
464 restricted to the intrusion margins where the assimilation of country rocks may have occurred

465 during a period of limited magma mixing. The immediate country rocks to the Fazenda  
466 Mirabela intrusion include metamorphosed black shales (now present as graphite- and pyrite-  
467 bearing gneisses) which are often considered to be sources of As, S, and other semimetals  
468 (e.g., Hutchinson and McDonald, 2008). Although there is no direct evidence for the  
469 assimilation of As-bearing crustal rocks at Fazenda Mirabela, such as the presence of  
470 sulfarsenides or As-bearing PGM concentrated around crustal xenoliths, it is difficult to  
471 understand how the distinct zoning of As in the intrusion could have been achieved  
472 otherwise. It is possible that the syn-hydrothermal processes associated with the heat of  
473 magma emplacement resulted in the devolatilization of the country rocks and subsequent  
474 release of As (Hutchinson and McDonald, 2008) which was then introduced into the intrusion  
475 margins. This process would not require large amounts of assimilation via melting of the  
476 country rocks.

477

#### 478 *BMS stringers and associated PGM*

479 Sulfide stringers with associated PGM extending from interstitial BMS characterize  
480 the mineralization in the Santa Rita ore zone. It appears that both the BMS and PGE have  
481 been distributed together into these stringers which originate from the interstitial BMS, as  
482 suggested by their close association.

483 One possible explanation for the formation of these sulfide stringers and their  
484 associated PGM is that they are the result of post-magmatic hydrothermal remobilization. At  
485 low temperatures (<500°C), PGE ions will most likely complex with bisulfide (HS<sup>-</sup>),  
486 however, bisulfide complexes are incapable of redistributing significant amounts of PGE  
487 unless fluid/rock ratios are very high with very effective depositional mechanisms (Hanley,  
488 2005). In contrast, at high temperatures (>500°C), chloride complexes are more likely to form  
489 (Hanley 2005). However, experiments by Wood and Normand (2008) demonstrate that  
490 unrealistically large amounts of oxidizing and acidic fluids are required to overcome the acid-  
491 and redox-buffering capacity of mafic, and by proxy ultramafic lithologies in order to  
492 mobilize palladium as a chloride complex.

493 It has been demonstrated that hydrothermal fluids may liberate PGE from their BMS  
494 hosts resulting in the formation of PGM. However, it is rare that the PGE are extensively  
495 remobilized and they are usually only transported very short distances (micrometers) in most  
496 cases (e.g., Prichard et al. 1994; Wang et al. 2008; Dare et al. 2010a; Prichard et al. 2013).  
497 Sulfur is typically much more mobile than the PGE, and in many examples where BMS and  
498 PGE have been affected by hydrothermal alteration, the BMS are remobilized or altered,  
499 resulting in either the exsolution of PGE in situ to form PGM associated with BMS or  
500 secondary phases (e.g., Prichard et al. 1994; Godel and Barnes, 2008a; 2008b; Prichard et al.  
501 2013), or the isolation of preexisting PGM in secondary phases (e.g., Sá et al., 2005).  
502 However, the opposite has also been demonstrated in the Platreef, where late stage fluids  
503 have remobilized the PGE into the footwall in tremolite, talc, and serpentine as low  
504 temperature PGM assemblages that are devoid of sulfur (Armitage et al., 2002; Hutchinson  
505 and Kinnaird, 2005). The Waterberg deposit, South Africa, which shows many features  
506 typical of a low pressure epithermal system (Armitage et al., 2007) is perhaps the only  
507 example where large scale PGE (platinum) remobilization has occurred and is an atypical  
508 case (McDonald et al., 1999).

509           There is some evidence to suggest that these BMS stringers and their associated PGM  
510 are the product of hydrothermal remobilization. Many of the BMS stringers are associated  
511 with serpentine (Fig. 9E) indicating that post-magmatic hydrothermal alteration is responsible  
512 for their formation. However, if the sulfides had been affected or remobilized by  
513 hydrothermal processes, their composition should include secondary sulfides or magnetite  
514 (e.g., Godel and Barnes, 2008a; 2008b; Prichard et al., 2013; Smith et al., 2014). This is not  
515 observed as the stringers are composed of pentlandite, pyrrhotite, and chalcopyrite. Many  
516 studies have demonstrated that Pd is far more mobile than Pt (e.g., Fuchs and Rose, 1974;  
517 Prichard et al., 1994; 2001; Seabrook et al., 2004; Barnes et al., 2008; Wang et al., 2008;  
518 Suárez et al., 2010), thus one might expect Pd-bearing PGM to be dominant in these sulfide  
519 stringers. However, the PGM in the stringers are similar to those in the interstitial BMS  
520 including both Pt-bearing tellurides (Fig. 9E-F) and sperrylite (Fig. 10D-E). Therefore there  
521 is no evidence for the preferential remobilization of Pd over Pt. Furthermore, semimetal-  
522 bearing PGM are very insoluble compounds (Wood, 2002). It is therefore very unlikely that  
523 preexisting PGM associated with the interstitial sulfides have been remobilized into the  
524 sulfide stringers in the Fazenda Mirabela intrusion.

525           An alternative mode of formation for these BMS stringers and their associated PGM  
526 is that they represent the migration and crystallization of late-stage, PGE-bearing,  
527 fractionated sulfide liquids. This has been proposed for the formation of PGM-bearing  
528 veinlets observed in the Stillwater Complex (Zientek, 2002) and emanating from an  
529 immiscible sulfide bleb in a dyke in Uruguay (Prichard et al., 2004b). However, the  
530 composition of these stringers should be dominated by the recrystallization products of ISS  
531 such as chalcopyrite and other Cu-rich sulfides given the known fractionation of sulfide  
532 liquids (e.g., Hawley, 1965; Keays and Crocket, 1970; Naldrett et al., 1982; Holwell and  
533 McDonald, 2010), but pentlandite and pyrrhotite stringers are commonly observed (Fig. 9E).

534           A mechanical process whereby the sulfide liquid was compressed by the gravity  
535 settling and compaction of crystallizing silicates in the magma chamber best accounts for all  
536 observed features of the BMS stringers and their associated PGM. This compression forced a  
537 portion of the sulfide liquid, which at this point was coalescing as interstitial blebs (Fig. 18A-  
538 B), outwards through the crystal pile in the direction of least resistance along the boundaries  
539 of olivine and pyroxene crystals, either replacing any interstitial silicate melt or migrating  
540 through solidified silicates along their grain boundaries (Mungall and Su, 2005) giving rise to  
541 the observed alignment of the sulfide stringers. In some cases, it appears that the sulfide  
542 liquid has fractured crystallized silicates during its migration offsetting preexisting cracks  
543 (Fig. 9F). The unfractionated sulfide liquid then cooled and crystallized to form MSS and ISS  
544 in situ at sites interstitial to silicates and in stringers (Fig. 18C). This accounts for the primary  
545 composition of the stringers and the consistent chemistry of both the sulfides and their  
546 associated PGM across both the interstitial sulfides and BMS stringers (Fig. 18D).

547

#### 548 *Variation in PGM abundance and the origin of high tenor BMS*

549           In the Santa Rita ore zone, semimetals are readily available (Fig. 7) resulting in the  
550 formation of abundant PGM, ~17 PGM per sample (thin section) studied, leaving the BMS  
551 PGE-poor (Table 5) as these elements exsolved from the sulfides during cooling to form  
552 PGM. The basal PGE anomaly in the S-poor dunite is semimetal-poor (Fig. 7), therefore

553 PGM do not readily form, with only ~5 PGM observed per sample (thin section) and the  
554 balance of PGE is retained in solid solution in high tenor sulfides (Table 5).

555 In the S- and semimetal-poor dunite, micro-scale sulfide-silicate graphic textures,  
556 very high PGE tenors, and an unusual BMS assemblage (pentlandite with minor chalcopyrite)  
557 cannot be explained by normal magmatic processes, particularly when compared to the Santa  
558 Rita ore zone. In an updated interpretation from that of Knight et al. (2011), we propose that  
559 small volumes of a magmatically derived, high temperature, volatile-rich (evidenced by the  
560 presence of phlogopite associated with sulfides exhibiting micro-scale sulfide-silicate graphic  
561 textures) fluid with a high oxygen fugacity ( $f_{O_2}$ ) interacted with the sulfides in the dunite after  
562 the crystallization of MSS, but before the crystallization of ISS. This interaction resulted in  
563 the removal of significant amounts of Cu-rich fractionated sulfide liquid into which Pt, Au,  
564 and the semimetals preferentially partitioned during the crystallization of MSS (Fig. 19A),  
565 whereas the IPGE, Rh, and Pd partitioned into MSS as it crystallized (e.g., Fleet et al., 1993;  
566 Li et al., 1996; Ballhaus et al., 2001; Mungall et al., 2005; Barnes et al., 2006; Godel et al.,  
567 2007; Helmy et al., 2007; Holwell and McDonald, 2007; Helmy et al., 2010; Osbahr et al.,  
568 2013; Cafagna and Jugo, 2016). These high temperature fluids appear to have redistributed  
569 the Cu-rich liquid (including the Pt, Au, and semimetals therein; Fig. 19B), upwards into the  
570 Santa Rita ore zone, evidenced by the abundance of Te-bearing PGM and the consistent  
571 increase in Pt and Au concentrations relative to the other PGE (Fig. 5 and 6). The continued  
572 interaction of this magmatic fluid with crystallized MSS appears to have removed sulfide via  
573 melting or dissolution of Fe-sulfide by oxidizing the Fe to  $Fe_3O_4$  while removing S as  $SO_2$  or  
574  $H_2S$ , resulting in the formation of magnetite (Fig. 19B) and other secondary minerals  
575 (Kinloch, 1982; Andersen, 2006) while creating the micro-scale sulfide-silicate graphic  
576 textures observed. The removal of Fe-sulfide resulted in Ni concentrations increasing in the  
577 remaining MSS, explaining the presence of pentlandite at the expense of pyrrhotite. The  
578 formation of PGM from MSS was extremely limited due to the removal of semimetals.  
579 Instead PGE remained in solid solution giving rise to high IPGE, Rh and Pd tenors in MSS,  
580 and subsequently pentlandite as it exsolved. During cooling, any remaining Cu-rich  
581 fractionated sulfide liquid crystallized to form ISS. Minor Au-Ag-Cu alloys and Te-bearing  
582 PGM exsolved on further cooling, while Pt diffused from ISS/chalcopyrite into pentlandite  
583 (Fig. 19C; Dare et al., 2010b; Piña et al., 2011).

584 These high temperature magmatic fluids appear to have interacted pervasively  
585 throughout the dunite, affecting all sulfides in this zone to some extent. However, there is  
586 evidence that this fluid was concentrated or channelized in some parts of the intrusion  
587 evidenced by the Pd-Cu alloy assemblage observed in borehole MBS604. In this localized  
588 basal zone of the intrusion, almost all of the fractionated Cu-rich sulfide liquid, including the  
589 Pt, Au, and semimetals therein, was removed (Fig. 19D) resulting in the formation of PGE-  
590 bearing alloys (predominantly Pd-Cu phases) in the absence of semimetals (Fig. 19E-F). The  
591 formation of alloys by desulfurization in other PGE-bearing systems has been reported, and is  
592 usually interpreted as a result of PGE being forced to exsolve during sulfur loss (Kinloch,  
593 1982, Andersen, 2006; Li and Ripley, 2006; Godel and Barnes, 2008a). One would expect  
594 that sulfides hosting Pd-Cu alloys in the Fazenda Mirabela intrusion would therefore be  
595 depleted in Pd (e.g., Godel and Barnes, 2008a), however, it is impossible to test this by LA-  
596 ICP-MS without also ablating these alloys.

597

598 *The presence of Pd in pentlandite*

599 Many natural and experimental studies suggest that Pd partitions with Pt and Au into  
600 fractionated sulfide melts during the crystallization of MSS and ISS (e.g., Fleet et al., 1993;  
601 Li et al., 1996; Peregoedova, 1998; Ballhaus et al., 2001; Mungall et al., 2005), however,  
602 significant concentrations of Pd are commonly identified in pentlandite. Some researchers  
603 have suggested that Pd may partition into a Cu-rich liquid, either ISS or a late stage  
604 immiscible sulfide melt (Barnes et al., 2006) and that it subsequently diffuses into pentlandite  
605 from chalcopyrite during cooling via subsolidus exchange (Dare et al., 2010b; Piña et al.,  
606 2011). However, this does not explain high Pd concentrations in pentlandite crystals that are  
607 isolated from other BMS where this diffusion process cannot occur (e.g., Osbahr et al., 2013)  
608 and recent experimental work demonstrates that in the absence of metalloid-rich phases, Pd  
609 partitions preferentially into MSS (Cafagna and Jugo, 2016). Significant concentrations of Pd  
610 must partition into MSS at an early magmatic stage to account for high Pd concentrations in  
611 isolated pentlandite crystals (Osbahr et al., 2013). In the S-poor dunite zone of the Fazenda  
612 Mirabela intrusion, it is clear that Pt, Au, and semimetals have been lost through their  
613 partitioning into a fractionated Cu-rich sulfide liquid which was then largely removed by high  
614 temperature magmatic fluids and redistributed into the Santa Rita ore zone above. However,  
615 Pd was not removed during this process which suggests that it partitioned into MSS as it  
616 crystallized from the sulfide liquid, and not into the fractionated Cu-rich sulfide liquid. The  
617 partitioning of Pd directly into MSS and subsequently pentlandite as it recrystallizes,  
618 eliminates the need to invoke Pd diffusion from fractionated Cu-rich sulfides.

619

620 *IPGE and cobalt in pyrite*

621 Concentrations of IPGE and Co in pyrite are being increasingly recognized and are  
622 again identified in pyrite from the Santa Rita ore zone in the Fazenda Mirabela intrusion.  
623 Cobalt concentrations in particular are very high and much more enriched when compared to  
624 the Co concentrations measured in pentlandite, pyrrhotite, and chalcopyrite. The discovery of  
625 PGE in pyrite has been noted previously with Pd identified in pyrite in the Keivitsansarvi Ni-  
626 Cu-PGE deposit in northern Finland (Gervilla and Kojonen, 2002), and Ru and Pt identified  
627 in pyrite in the Main Sulfide Zone of the Great Dyke in Zimbabwe (Oberthür et al., 1997).  
628 However, the genesis of such concentrations was not discussed in detail until recently.

629 Secondary pyrite commonly replaces pyrrhotite and pentlandite during post-magmatic  
630 hydrothermal alteration and it may inherit the PGE concentrations of these magmatic sulfides  
631 (Dare et al. 2011; Piña et al. 2012; 2013; Smith 2014; Duran et al. 2015; Piña et al. 2016). In  
632 these cases, the PGE concentrations in pyrite match those of the pyrrhotite and pentlandite it  
633 has replaced.

634 Alternatively, magmatic pyrite may exsolve from S-rich MSS in small quantities at  
635 temperatures below ~700°C (Naldrett et al., 1967). Pyrite that hosts higher concentrations of  
636 some PGE (typically the IPGE) than coexisting pyrrhotite and pentlandite is suggested to be  
637 magmatic, as it has not simply inherited the PGE content of the sulfides that secondary pyrite  
638 would have replaced (Lorand and Alard, 2011; Dare et al., 2011; Piña et al., 2012). However,  
639 these studies of PGE-bearing pyrite are in areas that have undergone extensive alteration,  
640 creating uncertainty in the process of pyrite formation; for example, the origin of PGE-

641 bearing idiomorphic pyrite in the Aguablanca Ni-Cu-PGE deposit is uncertain and may be  
642 either an exsolution product of MSS or the alteration product of pyrrhotite (Piña et al., 2012).

643 Furthermore, in the McCreedy East deposit at Sudbury, oscillatory zoning is observed  
644 in magmatic pyrite hosting higher IPGE concentrations than coexisting pyrrhotite and  
645 pentlandite, all of which are interpreted to have exsolved from MSS (Dare et al., 2011).  
646 However, this zoning is also considered a feature of secondary mineral replacement reactions,  
647 whereby pyrrhotite has been converted to pyrite (Duran et al., 2015). The enrichment of Co,  
648 Rh ± IPGE in pyrite could also be explained by a process of fluid-assisted solid-state  
649 diffusion from surrounding pentlandite and pyrrhotite, with semimetals, Pd, and Au  
650 introduced by the circulation of altering fluids (Piña et al., 2013; Duran et al., 2015).

651 Recent experimental work shows that pyrite exsolves from MSS during the cooling of  
652 a sulfide melt if the bulk S content is sufficiently high, and may incorporate significant  
653 amounts of Co, Ni, Ru, Rh, Os, Ir, and Pt, exhibiting a complex zonation of these elements  
654 similar to that observed in some natural occurrences (Cafagna and Jugo, 2016). This zoning is  
655 likely preserved due to slow diffusion rates in pyrite and can form during subsolidus reactions  
656 involving both MSS and ISS in the absence of hydrothermal processes (Cafagna and Jugo,  
657 2016).

658 Several lines of evidence suggest that the pyrite in the Fazenda Mirabela intrusion is  
659 primary and has exsolved from MSS. Unlike other occurrences where PGE ± Co bearing  
660 pyrite has been identified, the Fazenda Mirabela intrusion is almost completely unaltered  
661 with no textural or chemical evidence for any significant alteration or secondary sulfide  
662 remobilization in the Santa Rita ore zone. This is also evidenced by euhedral pyrite occurring  
663 in the cores of interstitial sulfides intergrown with pentlandite (Fig. 4C, 10A, 10C, and 11F).  
664 Secondary pyrite would typically replace pyrrhotite at the edges of sulfide blebs which is not  
665 observed. Furthermore, pyrite hosts individual IPGE in greater concentrations than both  
666 pyrrhotite and pentlandite (excluding Ru in pentlandite which has an average of 0.9 ppm  
667 compared to 0.8 ppm in pyrite) suggesting that it has not simply replaced these sulfides and  
668 inherited their PGE content; this is also supported by the Pd-poor nature of pyrite. If pyrite  
669 had replaced pentlandite (commonly found intergrown with pyrite), one would expect pyrite  
670 to host Pd concentrations similar to that of pentlandite. The zoning of PGE in pyrite whereby  
671 these elements are enriched in the rim where in contact with other BMS and depleted in the  
672 core may suggest that the PGE have diffused from adjacent sulfides, with zoning preserved  
673 due to very slow diffusion rates of Os (and presumably the other PGE) in pyrite (Brenan et  
674 al., 2000; Cafagna and Jugo, 2016). However, such zoning is not observed in LA-ICP-MS  
675 data where laser traces cut rim-core sections of pyrite crystals (Fig. 17A), suggesting that the  
676 IPGE and Co have immediately partitioned into pyrite during its exsolution from MSS. This  
677 study, amongst others, suggests that primary magmatic pyrite should be considered as a  
678 potential host for the IPGE and Rh, as well as Co, particularly in a system with high PGE  
679 tenors (e.g., a PGE-reef type setting).

680

681

## Conclusions

682 The understanding of PGE mineralization in the Fazenda Mirabela intrusion has been  
683 greatly improved by this study using a combination of geochemical and mineralogical



726 Ames, D.E., and Farrow, C.E.G., 2007, Metallogeny of the Sudbury mining camp, Ontario:  
727 Mineral Deposits Division, Geological Association of Canada Special Publication 5, p.  
728 329–350.

729 Armitage, P.E.B., McDonald I., Edwards S.J., and Manby G.M., 2002, Platinum-group  
730 element mineralization in the Platreef and calc-silicate footwall at Sandsloot, Potgietersrus  
731 District, South Africa: Applied Earth Science (Transactions of the Institute of Mining and  
732 Metallurgy B), v. 111, p. 36-45.

733 Armitage, P.E.B., McDonald, I., and Tredoux, M., 2007, A geological investigation of the  
734 Waterberg hydrothermal platinum deposit, Mookgophong, Limpopo Province, South Africa:  
735 Applied Earth Science (Transactions of the Institute of Mining and Metallurgy B), v. 116, p.  
736 113-129.

737 Ballhaus, C., and Sylvester, P., 2000, Noble Metal Enrichment Processes in the Merensky  
738 Reef, Bushveld Complex: Journal of Petrology, v. 41, p. 545-561.

739 Ballhaus, C., Tredoux, M., and Späth, A., 2001, Phase relations in the Fe-Ni-Cu-PGE-S  
740 system at magmatic temperature and application to massive sulphide ores of the Sudbury  
741 Igneous Complex: Journal of Petrology, v. 42, p. 1911-1926.

742 Barbosa, J.S.F., Gomes, L.C.C., Marinho, M.M., and Silva, F.C.A., 2003, Geologia do  
743 Segmento Sul do Orógeno Itabuna-Salvador-Curaçá: Revista Brasileira de Geociências, v.  
744 33, p. 33-48.

745 Barbosa, J.S.F., and Sabaté, P., 2004, Archean and Paleoproterozoic crust of the São  
746 Francisco Craton, Bahia, Brazil: geodynamic features: *Precambrian Research*, v. 133, p. 1-  
747 27.

748 Barnes, S.J., Osborne, G.A., Cook, D., Barnes, L., Maier, W.D., and Godel, B., 2011, The  
749 Santa Rita Nickel Sulfide Deposit in the Fazenda Mirabela Intrusion, Bahia, Brazil: Geology,  
750 Sulfide Geochemistry, and Genesis: *Economic Geology*, v. 106, p. 1083-1110.

751 Barnes, S-J., Cox, R.A., and Zientek, M.L., 2006, Platinum-group element, Gold, Silver and  
752 Base Metal distribution in compositionally zoned sulfide droplets from the Medvezky Creek  
753 Mine, Noril'sk, Russia: *Contributions to Mineralogy and Petrology*, v. 152, p. 187-200.

754 Barnes, S-J., Prichard, H.M., Cox, R.A., Fisher, P.C., and Godel, B., 2008, The location of  
755 the chalcophile and siderophile elements in platinum-group element ore deposits (a textural,  
756 microbeam and whole rock geochemical study): Implications for the formation of the  
757 deposits: *Chemical Geology*, v. 248, p. 295-317.

758 Brenan, J.M., Cherniak, D.J., and Rose, L.A., 2000, Diffusion of osmium in pyrrhotite and  
759 pyrite: implications for closure of the Re–Os isotopic system: *Earth and Planetary Science  
760 Letters*, v. 180, p. 399-413.

761 Cafagna, F., and Jugo, P.J., 2016, An experimental study on the geochemical behavior of  
762 highly siderophile elements (HSE) and metalloids (As, Se, Sb, Te, Bi) in a mss-iss-pyrite  
763 system at 650° C: A possible magmatic origin for Co-HSE-bearing pyrite and the role of  
764 metalloid-rich phases in the fractionation of HSE: *Geochimica et Cosmochimica Acta*, v.  
765 178, p. 233-258.

- 766 Dare, S.A.S., Barnes, S-J., Prichard, H.M., and Fisher, P.C., 2010a, The timing and formation  
767 of platinum-group minerals from the Creighton Ni-Cu-Platinum-Group Element sulfide  
768 deposit, Sudbury, Canada: Early crystallization of PGE-rich sulfarsenides: *Economic*  
769 *Geology*, v. 105, p. 1071-1096.
- 770 Dare, S.A.S., Barnes, S-J., and Prichard, H.M., 2010b, The distribution of platinum group  
771 elements (PGE) and other chalcophile elements among sulfides from the Creighton Ni-Cu-  
772 PGE sulfide deposit, Sudbury, Canada, and the origin of palladium in pentlandite:  
773 *Mineralium Deposita*, v. 45, p. 765-793.
- 774 Dare, S.A.S., Barnes, S-J., Prichard, H.M., and Fisher, P.C., 2011, Chalcophile and platinum-  
775 group element (PGE) concentrations in the sulfide minerals from the McCreedy East deposit,  
776 Sudbury, Canada, and the origin of PGE in pyrite: *Mineralium Deposita*, v. 46, p. 381-407.
- 777 Duran, C.J., Barnes, S-J., and Corkery, J.T., 2015, Chalcophile and platinum-group element  
778 distribution in pyrites from the sulfide-rich pods of the Lac des Iles Pd deposits, Western  
779 Ontario, Canada: Implications for post-cumulus re-equilibration of the ore and the use of  
780 pyrite compositions in exploration: *Journal of Geochemical Exploration*, v. 158, p. 223-242.
- 781 Ferreira Filho, C.F., Cunha, E.M., Lima, A.C., Cunha, J.C., 2013. Depósito de Níquel-Cobre  
782 Sulfetado de Santa Rita, Itagibá, Bahia, Brasil. *Série Arquivos Abertos*, v. 39, Companhia  
783 Baiana de Pesquisa Mineral, p., 1-59.
- 784 Fleet, M.E., Chrissyoulis, S.L., Stone, W.E., and Weisener, C.G., 1993, Partitioning of  
785 platinum-group elements and Au in the Fe - Ni - Cu - S system: experiments on the fractional  
786 crystallization of sulfide melt: *Contributions to Mineralogy and Petrology*, v. 115, p. 36-44.
- 787 Fuchs, W.A., and Rose, A.W., 1974, The geochemical behavior of platinum and palladium in  
788 the weathering cycle in the Stillwater Complex, Montana: *Economic Geology*, v. 69, p. 332-  
789 346.
- 790 Gervilla, F., and Kojonen, K., 2002, The platinum-group minerals in the upper section of the  
791 Keivitsansarvi Ni-Cu-PGE deposit, Northern Finland: *The Canadian Mineralogist*, v. 40, p.  
792 377-394. Godel B., and Barnes S-J., 2008a, Image analysis and composition of platinum-  
793 group minerals in the J-M Reef, Stillwater Complex: *Economic Geology*, v. 103, p. 637-651.
- 794 Godel B., and Barnes S-J., 2008b, Platinum-group elements in sulphide minerals and the  
795 whole rocks of the J-M Reef (Stillwater Complex): Implication for the formation of the reef:  
796 *Chemical Geology*, v. 248, p. 272-294.
- 797 Godel, B., Barnes, S-J., and Maier, W.D., 2007, Platinum-Group Elements in Sulphide  
798 Minerals, Platinum-Group Minerals, and Whole-Rocks of the Merensky Reef (Bushveld  
799 Complex, South Africa): Implications for the Formation of the Reef: *Journal of Petrology*, v.  
800 48, p. 1569-1604.
- 801 Hanley, J.J., 2005, The Aqueous Geochemistry of the Platinum Group Elements (PGE) in  
802 Surficial, Low-T Hydrothermal and High-T Magmatic-Hydrothermal Environments, in  
803 Mungall, J.E., ed., *Exploration for platinum-group element deposits: Mineralogical*  
804 *Association of Canada Short Course Series 35*, Oulu, Finland, p. 35-56.
- 805 Hawley, J.E., 1965, Upside-down zoning at Frood, Sudbury, Ontario: *Economic Geology*, v.  
806 60, p. 529-575.

- 807 Helmy, H.A., Ballhaus, C., Berndt, J., Bockrath, C., and Wohlgemuth-Ueberwassar, C., 2007,  
808 Formation of Pt, Pd and Ni tellurides: experiments in sulfide-telluride systems: Contributions  
809 to Mineralogy and Petrology, v. 153, p. 577-591.
- 810 Helmy, H.A., Ballhaus, C., Wohlgemuth-Ueberwassar, C., Fonseca, R.O.C., and Laurenz, V.,  
811 2010, Partitioning of Se, As, Sb, Te and Bi between monosulfide solid solution and sulfide  
812 melt - Application to magmatic sulfide deposits: *Geochimica et Cosmochimica Acta*, v. 74, p.  
813 6174-6179.
- 814 Holwell, D.A., and McDonald, I., 2007, Distribution of platinum-group elements in the  
815 Platreef at Overysel, northern Bushveld Complex: a combined PGM and LA-ICP-MS study:  
816 Contributions to Mineralogy and Petrology, v. 154, p. 171-190.
- 817 Holwell D.A., and McDonald I., 2010. A review of the behaviour of platinum-group elements  
818 within natural magmatic sulfide ore systems: The importance of semimetals in governing  
819 partitioning behaviour: *Platinum Metals Review*, v. 54, p. 26-36.
- 820 Hutchinson D., and Kinnaird J.A., 2005, Complex multistage genesis for the Ni-Cu-PGE  
821 mineralisation in the southern region of the Platreef, Bushveld Complex, South Africa:  
822 Applied Earth Science (Transactions of the Institute of Mining and Metallurgy B), v. 114, p.  
823 208-224.
- 824 Hutchinson, D., and McDonald, I., 2008, Laser ablation ICP-MS study of platinum-group  
825 elements in sulfides from the Platreef at Turfspruit, northern limb of the Bushveld Complex,  
826 South Africa: *Mineralium Deposita*, v. 43, p. 695-711.
- 827 Inwood, N., Smith, R., and Guzman, C., 2011, Santa Rita Project Technical Report, Mirabela  
828 Nickel Ltd.
- 829 Keays, R.R., and Crocket, J.H., 1970, A Study of Precious Metals in the Sudbury Nickel  
830 Irruptive Ores: *Economic Geology*, v. 65, p. 438-450.
- 831 Kinloch, E.D., 1982, Regional Trends in the Platinum-Group Mineralogy of the Critical Zone  
832 of the Bushveld Complex, South Africa: *Economic Geology*, v. 77, p. 1328-1347.
- 833 Knight, R.D., Prichard, H.M., McDonald, I., and Ferreira Filho, C.F., 2011, Platinum-group  
834 mineralogy of the Fazenda Mirabela intrusion, Brazil: the role of high temperature liquids  
835 and sulphur loss: Applied Earth Science (Transactions of the Institute of Mining and  
836 Metallurgy B), v. 120, p. 211-224.
- 837 Li, C., and Ripley, E.M., 2006, Formation of Pt-Fe alloy by desulfurization of Pt-Pd sulfide  
838 in the J-M Reef of the Stillwater Complex, Montana: *The Canadian Mineralogist*, v. 44, p.  
839 895-903.
- 840 Li, C., Barnes, S-J., Makovicky, E., Rose-Hansen, J., and Makovicky, M., 1996, Partitioning  
841 of nickel, copper, iridium, rhenium, platinum, and palladium between monosulfide solid  
842 solution and sulfide liquid: Effects of composition and temperature: *Geochimica et*  
843 *Cosmochimica Acta*, v. 60, p. 1231-1238.
- 844 Li, C., Ripley, E.M., and Naldrett, A.J., 2003, Compositional variations of olivine and sulfur  
845 isotopes in the Noril'sk and Talnakh intrusions, Siberia: Implications for ore-forming  
846 processes in dynamic magma conduits: *Economic Geology*, v. 98, p. 69-86.

847 Lodders, K., 2003, Solar system abundances and condensation temperatures of the elements:  
848 *Astrophysical Journal*, v. 591, p. 1220–1247.

849 Lorand, J-P., and Alard, O., 2010, Pyrite tracks assimilation of crustal sulfur in Pyrenean  
850 peridotites: *Contributions to Mineralogy and Petrology*, v. 101, p. 151-128.

851 Mariga, J., Ripley, E.M., and Li, C., 2006, Petrologic evolution of gneissic xenoliths in the  
852 Voisey's Bay Intrusion, Labrador, Canada: *Mineralogy, reactions, partial melting, and*  
853 *mechanisms of mass transfer: Geochemistry, Geophysics, Geosystems*, v. 7, doi:  
854 10.1029/2005GC001184.

855 McDonald, I., 2008, Platinum-group element and sulphide mineralogy in ultramafic  
856 complexes at western Andriamena, Madagascar: *Applied Earth Science (Transactions of the*  
857 *Institute of Mining and Metallurgy B)*, v. 117, p. 1-10.

858 McDonald, I., Ohnenstetter, D., Rowe, J.P., Tredoux, M., Patrick, R.A.D., and Vaughan,  
859 D.J., 1999, Platinum precipitation in the Waterberg deposit, Naboomspruit, South Africa:  
860 *South African Journal of Geology*, v. 102, p. 184-191.

861 Mungall, J.E., and Su, S., 2005, Interfacial tension between magmatic sulfide and silicate  
862 liquids: constraints on kinetics of sulfide liquation and sulfide migration through silicate  
863 rocks: *Earth and Planetary Science Letters*, v. 234, p. 135-149.

864 Mungall, J.E., Andrews, D.R.A., Cabri, L.J., Sylvester, P.J., and Tubrett, M., 2005,  
865 Partitioning of Cu, Ni, Au, and platinum-group elements between monosulfide solid solution  
866 and sulfide melt under controlled oxygen and sulfur fugacities: *Geochimica et Cosmochimica*  
867 *Acta*, v. 69, p. 4349-4360.

868 Naldrett, A.J., Craig, J.R., and Kullerud, G., 1967, The central portion of the Fe-Ni-S system  
869 and its bearing on pentlandite exsolution in iron-nickel sulfides ores: *Economic Geology*, v.  
870 62, p. 826-847.

871 Naldrett, A.J., Innes, D.G., Sowa, J., and Gorton, M.P., 1982, Compositional variations  
872 within and between 5 Sudbury ore-deposits: *Economic Geology*, v. 77, p. 1519-1534.

873 Naldrett, A.J., Lightfoot, P.C., Fedorenko, V.A., Doherty, W., and Gorbachev, N.S., 1992,  
874 Geology and geochemistry of intrusions and flood basalts of the Norilsk region, USSR, with  
875 implications for the origin of the Ni-Cu ores: *Economic Geology*, v. 87, p. 975-1004.

876 Oberthür, T., Cabri, L.J., Weiser, T.W., McMahon, G., and Müller, P., 1997, Pt, Pd and other  
877 trace elements in sulfides of the Main Sulfide Zone, Great Dike, Zimbabwe: A reconnaissance  
878 study: *The Canadian Mineralogist*, v. 35, p. 597-609.

879 Osbahr, I., Klemd, R., Oberthür, T., Brätz, H., and Schouwstra, R., 2013, Platinum-group  
880 element distribution in base-metal sulfides of the Merensky Reef from the eastern and  
881 western Bushveld Complex, South Africa: *Mineralium Deposita*, v. 48, p. 211-232.

882 Peregoedova, A.V., 1998, The Experimental Study of the Pt-Pd-Partitioning between  
883 Monosulfide Solid Solution and Cu-Ni-Sulfide Melt at 900–840°C [ext. abs]: *International*  
884 *Platinum Symposium, 8th, Johannesburg, South Africa, 1998, Extended Abstracts*, p. 325-  
885 327.

- 886 Peregoedova, A.V., Barnes, S-J., and Baker, D.R., 2004, The formation of Pt-Ir alloys and  
887 Cu-Pd-rich sulfide melts by partial desulfurization of Fe-Ni-Cu sulfides: results of  
888 experiments and implications for natural systems: *Chemical Geology*, v. 208, p. 247-264.
- 889 Peucat, J.J., Barbosa, J.S.F, Araújo, I.C.P., Paquette, J.L., Martin, H., Fanning, M., Menezes,  
890 A.B.L., Cruz, S., 2011, Geochronology of granulites from the south Itabuna-Salvador-Curaçá  
891 Block, São Francisco Craton (Brazil): Nd isotopes and U-Pb zircon ages: *Journal of South  
892 American Earth Sciences*, v. 31, p. 397-413.
- 893 Piña, R., Gervilla, F., Barnes, S-J., Ortega, L., and Lunar, R., 2012, Distribution of platinum-  
894 group and chalcophile elements in the Aguablanca Ni-Cu sulfide deposit (SW Spain):  
895 Evidence from a LA-ICP-MS study: *Chemical Geology*, v. 302–303, p. 61–75.
- 896 Piña, R., Gervilla, F., Barnes, S-J., Ortega, L., and Lunar, R., 2013, Partition Coefficients of  
897 Platinum Group and Chalcophile Elements Between Arsenide and Sulfide Phases as  
898 Determined in the Beni Bousera Cr-Ni Mineralization (North Morocco): *Economic Geology*,  
899 v. 108, p. 935-951.
- 900 Piña, R., Gervilla, F., Barnes, S-J., Oberthür, T., and Lunar, R., 2016, Platinum-group  
901 element concentrations in pyrite from the Main Sulfide Zone of the Great Dyke of  
902 Zimbabwe: *Mineralium Deposita*, DOI 10.1007/s00126-016-0642-3.
- 903 Prichard, H.M., Ixer, R.A., Lord, R.A., Maynard, J., and Williams, N., 1994, Assemblages of  
904 platinum-group minerals and sulphides in silicate lithologies and chromite-rich rocks within  
905 the Shetland Ophiolite: *The Canadian Mineralogist*, v. 32, p. 271-294.
- 906 Prichard, H.M., Sá, J.H.S., and Fisher, P.C., 2001, Platinum-group mineral assemblages and  
907 chromite composition in the altered and deformed Bacuri Complex, Amapá, Northeastern  
908 Brazil: *The Canadian Mineralogist*, v. 39, p. 377-396.
- 909 Prichard, H.M., Knight, R.D., Fisher, P.C., McDonald, I., Zhou, M-F., and Wang, C.Y.,  
910 2013, Distribution of platinum-group elements in magmatic and altered ores in the Jinchuan  
911 intrusion, China: an example of selenium remobilization by postmagmatic fluids: *Mineralium  
912 Deposita*, v. 48, p. 767-786.
- 913 Ripley, E.M., 1981, Sulfur Isotopic Studies of the Dunka Road Cu-Ni Deposit, Duluth  
914 Complex, Minnesota: *Economic Geology*, v. 76, p. 610-620.
- 915 Ripley, E.M., and Alawi, J.A., 1986, Sulfide mineralogy and chemical evolution of the  
916 Babbitt Cu-Ni deposit, Duluth Complex, Minnesota: *The Canadian Mineralogist*, v. 24, p.  
917 347-368.
- 918 Ripley, E.M., and Aljassar, T.J., 1987, Sulfur and oxygen isotope studies of melt-country  
919 rock interaction, Babbitt Cu-Ni deposit, Duluth Complex, Minnesota: *Economic Geology*, v.  
920 82, p. 87-107.
- 921 Ripley E.M., and Li, C., 2013, Sulfide Saturation in Mafic Magmas: Is External Sulfur  
922 Required for Magmatic Ni-Cu-(PGE) Ore Genesis?: *Economic Geology*, v. 108, p. 45-58.

923 Sá J.H.S., Barnes S.-J., Prichard H.P., and Fisher P.C., 2005, The Distribution of Base Metals  
924 and Platinum-Group Elements in Magnetitite and Its Host Rocks in the Rio Jacaré Intrusion,  
925 Northeastern Brazil: *Economic Geology*, v. 100, p. 333-348.

926 Samalens, N., Barnes, S.-J., and Sawyer, E.W., 2017, The role of black shales as a source of  
927 sulfur and semimetals in magmatic nickel-copper deposits: Example from the Partridge River  
928 Intrusion, Duluth Complex, Minnesota, USA: *Ore Geology Reviews*, v. 81, p. 173–187.

929 Seabrook, C.L., Prichard, H.M., and Fisher, P.C., 2004, Platinum-group minerals in the  
930 Raglan Ni-Cu-(PGE) sulfide deposit, Cape Smith, Quebec, Canada: *The Canadian*  
931 *Mineralogist*, v. 42, p. 485-497.

932 Smith, J.W., Holwell, D.A., and McDonald, I., 2014, Precious and base metal geochemistry  
933 and mineralogy of the Grasvalley Norite-Pyroxenite-Anorthosite (GNPA) member, northern  
934 Bushveld Complex, South Africa: implications for a multistage emplacement: *Mineralium*  
935 *Deposita*, v. 49, p. 667-692.

936 Suárez, S., Prichard, H.M., Velasco, F., Fisher, P.C., and McDonald, I., 2010, Alteration of  
937 platinum-group minerals and dispersion of platinum-group elements during progressive  
938 weathering of the Aguablanca Ni-Cu deposit, SW Spain: *Mineralium Deposita*, v. 45, p. 331-  
939 350.

940 Wang, C.Y., Prichard, H.M., Zhou, M-F., and Fisher, P.C., 2008, Platinum-group minerals  
941 from the Jinbaoshan Pd-Pt deposit, SW China: evidence for magmatic origin and  
942 hydrothermal alteration: *Mineralium Deposita*, v. 43, p. 791-803.

943 Wood, S.A., 2002, The aqueous geochemistry of the platinum-group elements with  
944 applications to ore deposits, in Cabri, L.J., ed., *The Geology, Geochemistry, Mineralogy and*  
945 *Mineral Beneficiation of the Platinum-group elements: Canadian Institute of Mining,*  
946 *Metallurgy and Petroleum, Montreal, Special Volume 54*, p. 211-249.

947 Wood S.A., and Normand C., 2008, Mobility of palladium chloride complexes in mafic  
948 rocks: insights from a flow-through experiment at 25 °C using air-saturated, acidic, and Cl-  
949 rich solutions: *Mineralogy and Petrology*, v. 92, p. 81-97.

950 Zientek, M.J., Cooper, R.W., Corson, S.R., and Geraghty, E.P., 2002, Platinum-group  
951 elements mineralization in the Stillwater Complex, Montana, in Cabri, L.J., ed., *The*  
952 *Geology, Geochemistry, Mineralogy and Mineral Beneficiation of the Platinum-group*  
953 *elements: Canadian Institute of Mining, Metallurgy and Petroleum, Montreal, Special*  
954 *Volume 54*, p. 459-481.

955

956

957

958

959

960

961 Table Captions:

962 Table 1: Depth, dip and azimuth information for all boreholes sampled from the central,  
963 northern and southern zones of the Fazenda Mirabela intrusion.

964 Table 2: Whole-rock semimetal and S concentrations for all samples studied from the  
965 southern zone boreholes MBS565 and MBS569. Abbreviations: Ol = olivine.

966 Table 3: Numbers of different platinum-group and precious metal minerals, sorted by type,  
967 identified from each zone of the intrusion (central, northern and southern) with the localized  
968 Pd-Cu alloy assemblage listed separately. Abbreviations: - = not detected

969 Table 4: Selective quantitative analyses and derived formulae of platinum-group and precious  
970 metal minerals from the northern and southern zones of the intrusion. Abbreviations: - = none  
971 observed

972 Table 5: Laser ablation-ICP-MS data for chalcopyrite, pentlandite, pyrrhotite, pyrite and  
973 BMS mixtures from the Santa Rita ore zone and basal PGE anomaly. Abbreviations: Cpy =  
974 chalcopyrite, Pn = pentlandite, Po = pyrrhotite, Py = pyrite, *n* = number of minerals analyzed,  
975 Ave = mean, Min = minimum value, Max = maximum value. \* indicates isotopes where  
976 corrections have been applied for polyatomic or isobaric interferences.

977

978 Figure Captions:

979 Fig. 1. A. Map showing the location of the Fazenda Mirabela intrusion and simplified  
980 geology of the southern portion of the Itabuna-Salvador-Curaçá belt (modified after Barbosa  
981 et al., 2003; Barbosa and Sabaté, 2004). B. Map showing context and location of A within the  
982 major South American tectonic units. AC = Amazonian Craton; SF = São Francisco Craton.

983 Fig. 2. Geological map of the Fazenda Mirabela intrusion showing the location (projected to  
984 the surface) of the boreholes sampled; MBS209 and MBS158 from the northern zone,  
985 MBS604 and MBS605 from the central zone, and MBS565 and MBS569 from the southern  
986 zone (modified after Inwood et al., 2011). The W-E geological section, representative of the  
987 central zone of the intrusion, shows the location of borehole MBS604 (modified after Ferreira  
988 Filho et al., 2013).

989 Fig. 3. Geochemical profile of borehole MBS565 (southern zone) showing the position of the  
990 samples studied. The Santa Rita ore zone is defined by elevated S, Pt, and Pd concentrations  
991 (samples PTSR51-56). The basal PGE anomaly is present in dunite (samples PTSR58-60)  
992 and is characterized by elevated PGE, predominantly Pd, while remaining S-poor.

993 Fig. 4. Transmitted and reflected light photomicrographs, and back-scattered electron images  
994 showing the silicate and sulfide petrography of the Mirabela intrusion. A and B. Olivine and  
995 orthopyroxene with interstitial BMS demonstrating unaltered magmatic textures and  
996 minerals. C. Detailed image of BMS showing the relationship between pentlandite, euhedral  
997 pyrite, and chalcopyrite. D. Example of small finely disseminated sulfides in the S-poor  
998 dunite hosting the basal PGE anomaly. E and inset F. Example of micro-scale sulfide-silicate  
999 graphic textures resembling symplectites. BMS = base metal sulfides, Cpy = chalcopyrite, Cr  
1000 = chromite, Opx = orthopyroxene, Ol = olivine, Pn = pentlandite, Py = pyrite, Sil = silicates.

1001 Fig. 5. Diagram showing the variation in chondrite normalized PGE profiles within the  
1002 Fazenda Mirabela stratigraphy using samples from borehole MBS569. Pattern A. Negative  
1003 Pd anomalies observed in the Santa Rita ore zone. Pattern B. Positive slopes without any  
1004 significant anomalies in the transition between the Santa Rita ore zone and basal PGE  
1005 anomaly. Pattern C. Positive Pd and negative Au (and Pt) anomalies in S-poor dunite samples  
1006 from the basal PGE anomaly.

1007 Fig. 6. PGE ratio plots showing the variation in Pt, Pd, and Au concentrations between  
1008 orthopyroxenite-harzburgite samples typically hosting the Santa Rita ore zone and S-poor  
1009 dunite samples hosting the basal PGE anomaly. A. Variation in Pt/Pd ratios in dunite samples  
1010 from the basal PGE anomaly and overlying orthopyroxenite samples. B. Variation in Au/Pd  
1011 ratios in dunite samples from the basal PGE anomaly and overlying orthopyroxenite samples.

1012 Fig. 7. Plot demonstrating the significant correlation between Te (as a proxy for all  
1013 semimetals) and S in whole-rock samples from boreholes MBS565 and MBS569 in the  
1014 southern zone of the intrusion.

1015 Fig. 8. Schematic diagram showing the location of the different PGM assemblages identified;  
1016 (i) predominately (Pt,Pd,Ni)(Fe,Bi,Te)<sub>2</sub> in the central zone, (ii) (Pt,Pd,Ni,Cu)(Fe,Bi,Te)<sub>2</sub> with  
1017 As-bearing PGM at the margins of the intrusion, and (iii) the localized Pd-Cu alloy  
1018 assemblage in the S-poor dunite in borehole MBS604 only.

1019 Fig. 9. Representative back-scattered electron images showing PGE tellurides from the  
1020 northern and southern zones of the Fazenda Mirabela intrusion. A. Rounded Pd-Pt telluride  
1021 within chalcopyrite. B. Rounded Ni-Pd telluride within pentlandite. C. Lath shaped Ni-Pt-Pd  
1022 telluride within BMS, and crossing pyrite and chalcopyrite. D. Lath shaped Pt telluride at the  
1023 edge of chalcopyrite and in contact with pyroxene. E. Pyrrhotite stringer hosting Pt-Ni-Fe  
1024 telluride, both enclosed by a serpentine veinlet cutting olivine. F. Chalcopyrite stringer  
1025 connecting to an interstitial sulfide bleb (pentlandite) hosting Ni-Pt-Pd telluride. Cpy =  
1026 chalcopyrite, Ol = olivine, Pn = pentlandite, Po = pyrrhotite, Py = pyrite, Pyx = pyroxene,  
1027 Serp = serpentine.

1028 Fig. 10. Representative back-scattered electron images showing As-bearing PGM from the  
1029 northern and southern zones of the Fazenda Mirabela intrusion. A. Sperrylite within  
1030 pentlandite. B. Sperrylite within and at the edge of pentlandite and in contact with pyroxene.  
1031 C. Sperrylite associated with chalcopyrite, pyroxene and serpentine. D. Partial sperrylite  
1032 stringer at the termination of an interstitial sulfide bleb. E. Sperrylite associated with BMS  
1033 stringer (out of frame) cutting pyroxene. F. Platarsite-irarsite within pentlandite associated  
1034 with pyrite. Cpy = chalcopyrite, Cr = chromite, Pn = pentlandite, Py = pyrite, Pyx =  
1035 pyroxene, PtAs<sub>2</sub> = sperrylite, (Pt,Ir)AsS = platarsite-irarsite, Serp = serpentine.

1036 Fig. 11. Ternary diagram showing the variation in Ni, Pd, and Pt concentrations in PGE-  
1037 tellurides. Atomic weight proportions plotted from semi-quantitative data derived from the  
1038 SEM.

1039 Fig. 12. Representative back-scattered electron images showing accessory phases in the Santa  
1040 Rita ore zone and PGM from the localized Pd-Cu alloy assemblage in the basal PGE anomaly  
1041 in the central zone (MBS604 only). A. Hessite within and at the margins of pentlandite, and  
1042 in contact with pyroxene. B. Hessite within and at the margins of pentlandite and pyrrhotite,  
1043 and in contact with serpentine. C. Electrum with Cu and Fe within and at the edge of

1044 chalcopyrite, and in contact with olivine and serpentine. D. Native Au within serpentine. E.  
1045 and inset F. Pd-Cu alloys within pentlandite exhibiting micro-scale sulfide-silicate graphic  
1046 textures that resemble symplectites. Ag<sub>2</sub>Te = hessite, Cpy = chalcopyrite, Cr = chromite, Ol =  
1047 olivine, Mgt = magnetite, Pn = pentlandite, Po = pyrrhotite, Pyx = pyroxene, Serp =  
1048 serpentine.

1049 Fig. 13. Histograms showing the percentage of different platinum-group and precious metal  
1050 minerals types identified at different textural sites. A. All zones of the intrusion. B. The  
1051 northern and southern zones of the intrusion only. The addition of central zone data does not  
1052 significantly alter the histogram pattern demonstrating that the mineral associations are very  
1053 similar, except in the case of the Pd-Cu alloy assemblage that is absent in the marginal zones.

1054 Fig. 14. Pie charts showing the distribution of different platinum-group and precious metal  
1055 minerals in the central zone versus the northern and southern zones of the intrusion. A and B.  
1056 Proportion of the different PGM and PMM identified in the central zone (excluding the Pd-  
1057 Cu alloy assemblage) calculated by the number and total area observed, respectively. C and  
1058 D. Proportion of the different PGM and PMM identified in the northern and southern zones  
1059 calculated by the number and total area observed, respectively. E and F. Proportion of the  
1060 different PGM and PMM identified in the localized Pd-Cu alloy assemblage calculated by the  
1061 number and total area observed, respectively.

1062 Fig. 15. Histogram showing the difference in platinum-group and precious metal mineral size  
1063 (in  $\mu\text{m}^2$ ) from the Santa Rita ore zone and the basal PGE anomaly in the S-poor dunite.

1064 Fig. 16. Stacked column plots showing the average concentrations of PGE in different  
1065 sulfides determined by LA-ICP-MS. A. Sulfides analyzed from the Santa Rita ore zone. B.  
1066 Sulfides analyzed from the basal PGE anomaly in the S-poor dunite.

1067 Fig. 17. Plots of time resolved spectra from LA-ICP-MS traces through BMS from the  
1068 Fazenda Mirabela intrusion. A. Pyrite-pentlandite from the Santa Rita ore zone with pyrite  
1069 hosting significant Co, Os, and Ru. B. Pentlandite from the basal PGE anomaly in the S-poor  
1070 dunite hosting high concentrations of Ir, Pd, and Pt.

1071 Fig. 18. Schematic diagram demonstrating the formation of BMS stringers and their  
1072 associated PGM. Temperatures are based on the crystallization temperatures of MSS and ISS,  
1073 and exsolution temperatures of pentlandite, pyrrhotite, and chalcopyrite. A. Sulfide liquid  
1074 coalesces as interstitial blebs to olivine and pyroxene. B. Compression from the growing  
1075 silicate crystal pile forces the sulfide liquid into stringers along silicate grain boundaries in  
1076 the direction of least resistance. C. The sulfide liquid crystallizes to form MSS and ISS. D.  
1077 These phases re-crystallize to form pentlandite, pyrrhotite, pyrite, and chalcopyrite during  
1078 subsolidus cooling. PGM exsolve from interstitial sulfides and BMS stringers during further  
1079 cooling. Ol = olivine, Pn = pentlandite, Po = pyrrhotite, Py = pyrite, Pyx = pyroxene.

1080 Fig. 19. Schematic diagram showing the formation of micro-scale sulfide-silicate graphic  
1081 textures resembling symplectites and associated PGM from the basal PGE anomaly in the S-  
1082 poor dunite. Temperatures are based on the crystallization temperatures of MSS and ISS, and  
1083 exsolution temperatures of pentlandite, pyrrhotite, and chalcopyrite. A. Platinum, Au, and the  
1084 semimetals partition into a fractionated Cu-rich sulfide liquid that forms during the  
1085 crystallization of MSS. B. Small volumes of high temperature, volatile-rich, magmatic fluid  
1086 with a high oxygen fugacity ( $f_{\text{O}_2}$ ) removes a significant portion of this Cu-rich liquid

1087 including the Pt, Au, and semimetals therein (and redistributes these elements into the  
1088 overlying Santa Rita ore zone) replacing it with magnetite and phlogopite while the  
1089 remainder crystallizes to form minor ISS. Further fluid/MSS interaction results in the  
1090 formation of micro-scale sulfide-silicate graphic textures and FeS is partially-totally replaced  
1091 by magnetite. C. Pentlandite and minor chalcopyrite recrystallizes from MSS and ISS,  
1092 respectively, and small numbers of PGE-bearing minerals exsolve from the sulfides utilizing  
1093 any remaining semimetals during subsolidus cooling; the majority of PGE are retained in  
1094 solid solution in high tenor sulfides. D. In MBS604, high temperature fluids are channelized  
1095 and almost all of the Cu-rich sulfide liquid is removed and replaced with phlogopite, minor  
1096 bornite and magnetite. E. Further fluid/MSS interaction results in the formation of micro-  
1097 scale sulfide-silicate graphic textures and FeS is partially-totally replaced by magnetite. F.  
1098 Pentlandite recrystallizes from MSS and PGE exsolve from this sulfide phase primarily in the  
1099 form of alloys in the absence of semimetals. Bn = bornite, Cpy = chalcopyrite, Mgt =  
1100 magnetite, Ol = olivine, Phlog = phlogopite, Pn = pentlandite.

1101

1102

1103

1104

1105

1106

1107

1108

1109

1110

1111

1112

1113

1114

1115

1116

1117

1118

1119

1120

1121

1122 Tables:

1123 Table 1

Borehole	Depth (m)	Dip	Azimuth
MBS604	1072	68°	270°
MBS605	1067	69°	270°
MBS209	356	60°	270°
MBS158	368	60°	270°
MBS565	630	61°	270°
MBS569	761	60°	270°

1124

1125

1126 Table 2

Borehole	Sample No.	Lithology	As ppm	Bi ppm	Sb ppm	Te ppm	S wt. %
MBS565	PTSR0050	Websterite	0.20	< 0.02	< 0.02	< 0.02	0.15
MBS565	PTSR0051	Orthopyroxenite	0.80	0.05	< 0.02	0.72	0.47
MBS565	PTSR0052	Orthopyroxenite	0.70	0.07	0.03	0.89	0.70
MBS565	PTSR0053	OI Orthopyroxenite	0.50	0.03	0.02	0.63	0.28
MBS565	PTSR0054	Harzburgite	0.20	< 0.02	0.08	0.26	0.14
MBS565	PTSR0055	Harzburgite	1.80	0.14	< 0.02	2.40	1.41
MBS565	PTSR0056	Harzburgite	1.50	0.15	0.03	2.46	1.40
MBS565	PTSR0057	Harzburgite	0.60	< 0.02	1.10	0.40	0.14
MBS565	PTSR0058	Dunite	0.20	< 0.02	0.03	0.19	0.05
MBS565	PTSR0059	Dunite	0.30	< 0.02	< 0.02	0.10	0.04
MBS565	PTSR0060	Dunite	0.20	< 0.02	0.02	0.08	0.04
MBS569	PTSR0061	Gabbro	0.20	< 0.02	0.04	0.02	0.08
MBS569	PTSR0062	Websterite	0.40	< 0.02	0.05	0.03	0.23
MBS569	PTSR0063	Orthopyroxenite	0.70	0.06	0.02	0.72	0.70
MBS569	PTSR0064	OI Orthopyroxenite	1.50	0.21	0.06	2.77	1.84
MBS569	PTSR0065	OI Orthopyroxenite	0.70	0.06	0.02	1.23	0.60
MBS569	PTSR0066	OI Orthopyroxenite	4.10	0.13	0.08	1.52	0.84
MBS569	PTSR0067	Harzburgite	1.10	< 0.02	< 0.02	0.13	0.06
MBS569	PTSR0068	Harzburgite	1.00	< 0.02	< 0.02	0.30	0.15
MBS569	PTSR0069	Harzburgite	0.50	0.02	< 0.02	0.65	0.34
MBS569	PTSR0070	Dunite	< 0.1	< 0.02	< 0.02	0.12	0.06
MBS569	PTSR0071	Dunite	0.30	< 0.02	< 0.02	0.04	0.02
MBS569	PTSR0072	Dunite	0.10	< 0.02	< 0.02	0.02	0.02

1127

1128

1129

1130

1131 Table 3

Zone	Platinum-group and precious metal mineral types							Total
	(Ni,Cu,Pt,Pd) (Fe,Bi,Te) <sub>2</sub>	Ag-Pd-Te	Ag <sub>2</sub> Te	(Pt,Fe,Rh)As <sub>2</sub>	(Ir,Pt,Rh)AsS	Pd-(Cu,Pb)	Au-(Ag,Cu,Fe)	
Central	156	0	29	2	1	0	8	196
Northern	183	16	41	49	11	0	9	309
Southern	139	5	27	20	7	1	14	213
Localised PGE alloy	2	0	0	2	2	15	0	21
Total	480	21	97	73	21	16	31	739

1132

1133

1134

1135

1136

1137

1138

1139

1140

1141

1142

1143

1144

1145 Table 4

Borehole	Sample	Mineral No.	Quantitative analyses (wt. %)										Mineral composition
			Fe	Ni	Cu	As	Pd	Ag	Te	Pt	Bi	Total	
MBS158	PTSR-40	A1	-	18.97	-	-	0.41	-	80.52	-	-	99.90	(Ni <sub>1.01</sub> Pd <sub>0.01</sub> ) <sub>1.02</sub> Te <sub>1.98</sub>
MBS158	PTSR-40	H1	-	8.89	-	-	0.85	-	69.40	21.16	-	100.30	(Ni <sub>0.56</sub> Pt <sub>0.40</sub> Pd <sub>0.03</sub> ) <sub>0.99</sub> Te <sub>2.01</sub>
MBS605	PTSR-22	B1	2.09	12.38	-	-	4.09	-	70.07	11.34	-	99.97	(Ni <sub>0.71</sub> Pt <sub>0.19</sub> Pd <sub>0.13</sub> ) <sub>1.03</sub> (Te <sub>1.84</sub> Fe <sub>0.13</sub> ) <sub>1.97</sub>
MBS604	PTSR-07	F1	2.57	6.28	-	-	10.80	-	66.36	13.21	-	99.22	(Ni <sub>0.38</sub> Pd <sub>0.36</sub> Pt <sub>0.24</sub> ) <sub>0.98</sub> (Te <sub>1.85</sub> Fe <sub>0.17</sub> ) <sub>2.02</sub>
MBS158	PTSR-46	H1	0.96	5.42	-	-	9.55	-	68.51	15.69	-	100.13	(Ni <sub>0.34</sub> Pd <sub>0.33</sub> Pt <sub>0.30</sub> ) <sub>0.97</sub> (Te <sub>1.97</sub> Fe <sub>0.06</sub> ) <sub>2.03</sub>
MBS158	PTSR-40	K1	1.35	19.72	-	-	-	-	79.74	-	-	100.81	Ni <sub>1.02</sub> (Te <sub>1.90</sub> Fe <sub>0.08</sub> ) <sub>1.98</sub>
MBS158	PTSR-40	I1	1.64	18.65	-	-	-	-	76.99	-	2.71	99.99	Ni <sub>0.99</sub> (Te <sub>1.88</sub> Fe <sub>0.09</sub> Bi <sub>0.04</sub> ) <sub>2.01</sub>
MBS158	PTSR-46	F1	-	4.41	-	-	6.13	-	65.68	24.25	-	100.47	(Pt <sub>0.48</sub> Ni <sub>0.29</sub> Pd <sub>0.23</sub> ) <sub>1.00</sub> Te <sub>2.00</sub>
MBS158	PTSR-40	E1	-	-	-	-	-	62.02	37.91	-	-	99.93	Ag <sub>1.98</sub> Te <sub>1.02</sub>
MBS158	PTSR-40	M1	-	-	-	-	-	61.02	38.31	-	-	99.33	Ag <sub>1.96</sub> Te <sub>1.04</sub>
MBS565	PTSR-58	A1	-	-	-	42.60	-	-	-	57.12	-	99.72	Pt <sub>1.02</sub> As <sub>1.98</sub>
MBS569	PTSR-68	F1	-	-	-	44.27	-	-	-	56.67	-	100.94	Pt <sub>0.99</sub> As <sub>2.01</sub>
MBS569	PTSR-68	G1	-	-	34.62	-	-	-	65.93	-	-	100.55	Cu <sub>1.03</sub> Te <sub>0.97</sub>

1146

1147

1148

1149

1150

1151

1152

1153

1154

1155 Table 5

Mineral analyzed		Element	<sup>59</sup> Co ppm	<sup>189</sup> Os ppm	<sup>193</sup> Ir ppm	<sup>99</sup> Ru* ppm	<sup>103</sup> Rh* ppm	<sup>195</sup> Pt ppm	<sup>105</sup> Pd ppm
Sulfides from the Santa Rita ore zone									
Cpy	<i>n</i> =48	Ave	201.22	0.03	<0.02	0.14	<0.10	0.05	0.27
		Min	0.09	<0.02	<0.02	<0.05	<0.10	<0.02	<0.20
		Max	1887.00	0.80	0.03	0.63	0.10	0.58	1.58
Pn	<i>n</i> =95	Ave	3026.20	0.52	0.09	0.91	0.11	0.03	2.31
		Min	670.00	<0.02	<0.02	<0.05	<0.10	<0.02	<0.20
		Max	7313.00	4.49	0.91	6.36	1.13	0.73	12.97
Po	<i>n</i> =36	Ave	65.57	0.55	0.11	0.58	0.04	0.07	0.01
		Min	1.29	0.00	<0.02	<0.05	<0.10	<0.02	<0.20
		Max	615.20	3.80	0.90	5.73	1.03	1.58	0.52
Py	<i>n</i> =38	Ave	16671.29	0.61	0.18	0.78	0.14	0.03	0.12
		Min	8569.00	<0.02	<0.02	<0.05	<0.10	<0.02	<0.20
		Max	32030.00	2.16	1.00	3.68	0.77	0.14	1.52
Sulfides from the basal PGE anomaly in the S-poor dunite									
Cpy	<i>n</i> =3	Ave	515.71	<0.02	0.07	0.06	<0.10	0.08	8.81
		Min	18.84	0.00	<0.02	<0.05	<0.10	<0.02	0.52
		Max	1346.00	0.00	0.12	0.12	<0.10	0.24	15.90
Pn	<i>n</i> =27	Ave	5913.33	4.22	1.74	6.28	4.33	4.33	42.47
		Min	2416.00	<0.02	<0.02	<0.05	<0.10	<0.02	3.88
		Max	9761.00	38.25	28.69	59.13	36.15	28.89	254.30
Pn-Cpy mix	<i>n</i> =8	Ave	5561.50	1.16	0.57	3.33	2.21	2.57	42.42
		Min	1367.00	<0.02	<0.02	<0.05	<0.10	<0.02	0.80
		Max	8910.00	5.18	2.61	11.48	8.82	14.70	124.89
Py	<i>n</i> =2	Ave	10915.00	3.52	1.57	2.80	<0.10	<0.02	0.37
		Min	9920.00	0.96	0.67	<0.05	<0.10	<0.02	0.26
		Max	11910.00	6.08	2.48	5.61	<0.10	<0.02	0.49
Pn-Py mix	<i>n</i> =1	n/a	5750.00	0.30	27.87	1.37	0.68	12.50	570.40
Pn-Py-Cpy mix	<i>n</i> =1	n/a	3245.00	0.04	18.68	1.63	<0.10	6.20	371.70

1156

1157

1158

1159

1160

1161

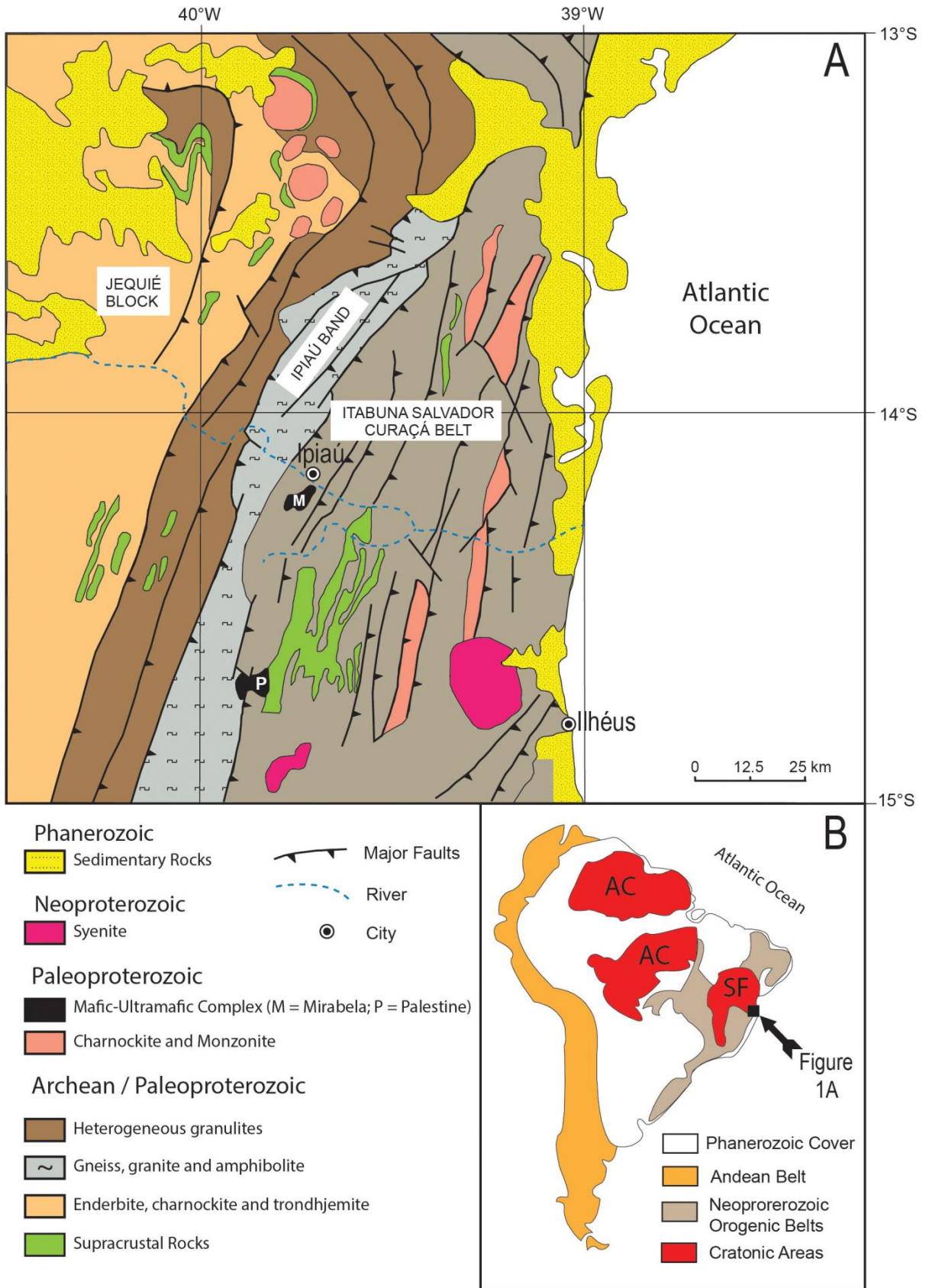
1162

1163

1164

1165

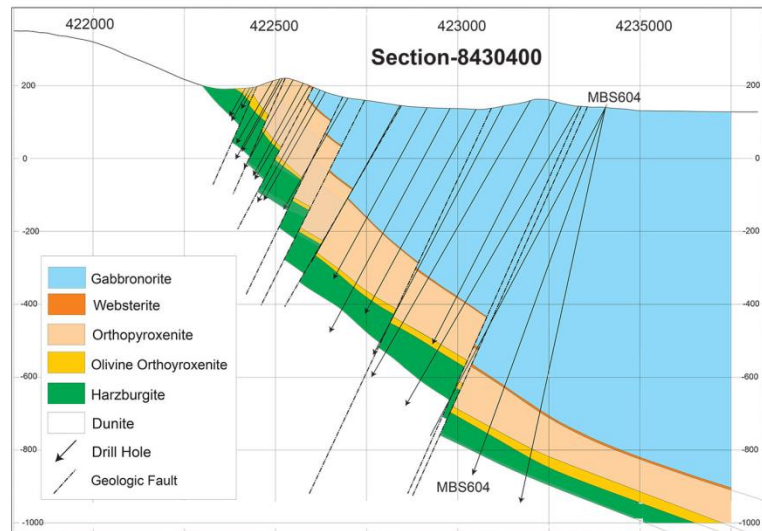
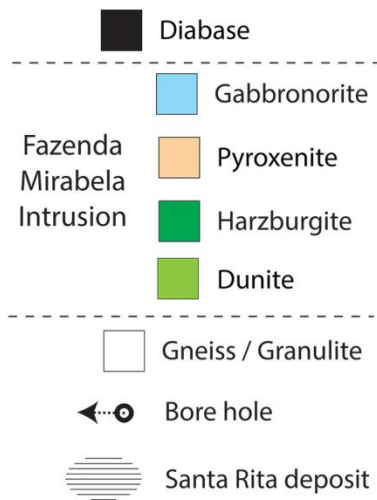
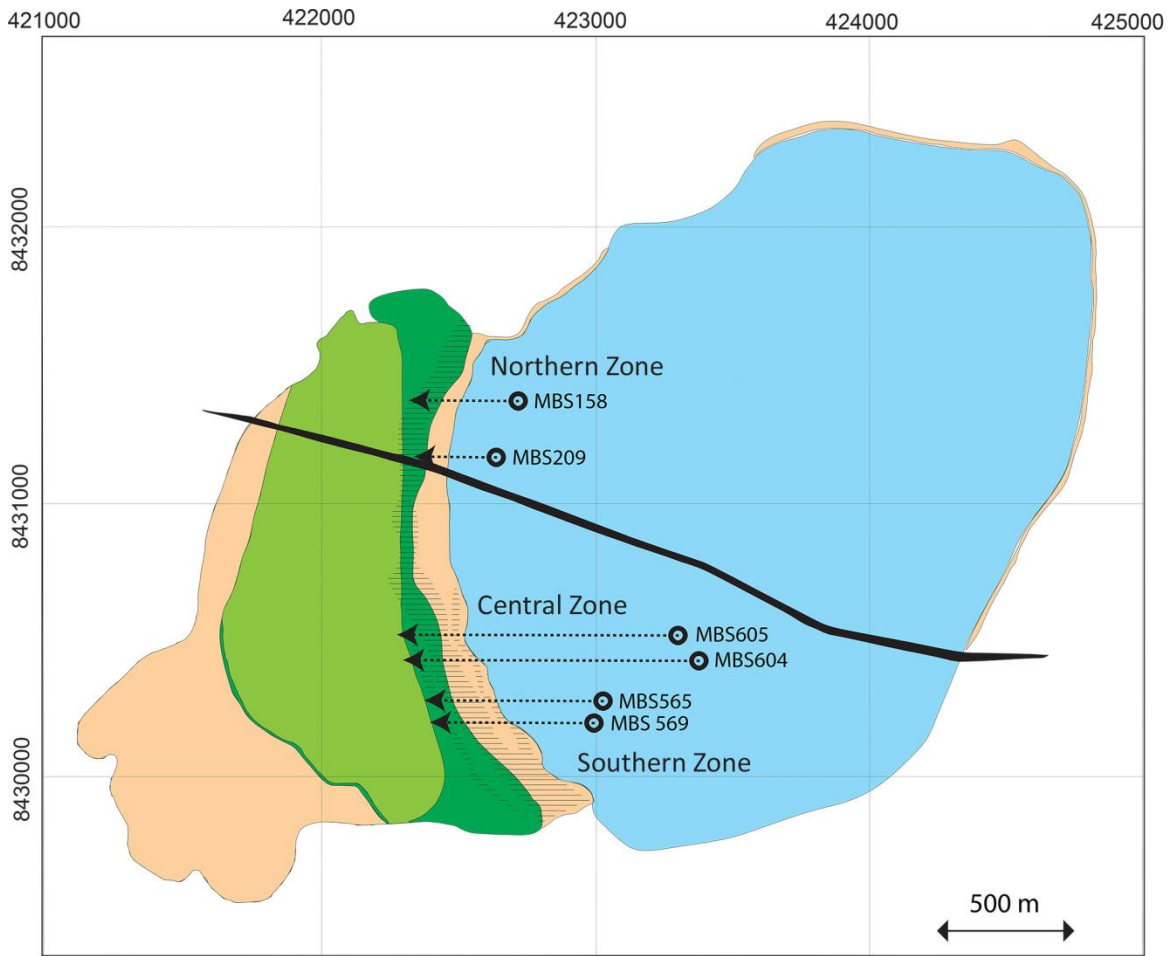
1166 Fig. 1



1167

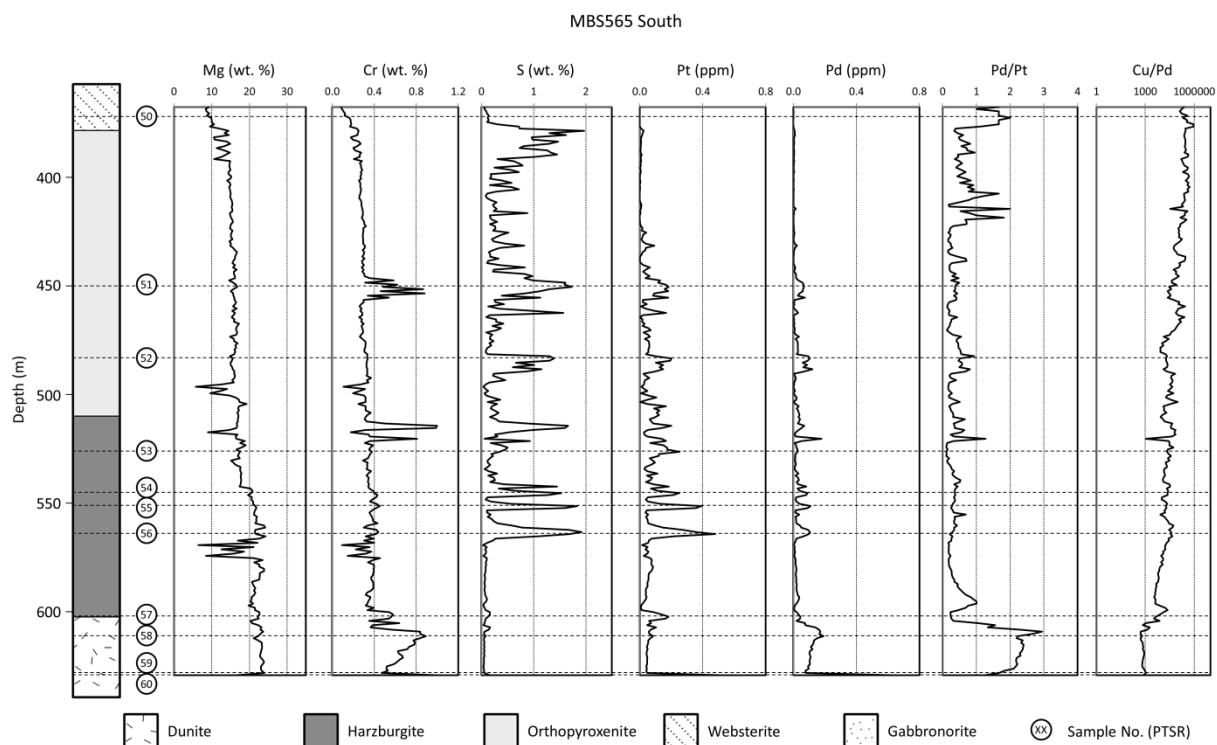
1168

1169 Fig. 2



1170  
1171  
1172  
1173  
1174

1175 Fig. 3



1176

1177

1178

1179

1180

1181

1182

1183

1184

1185

1186

1187

1188

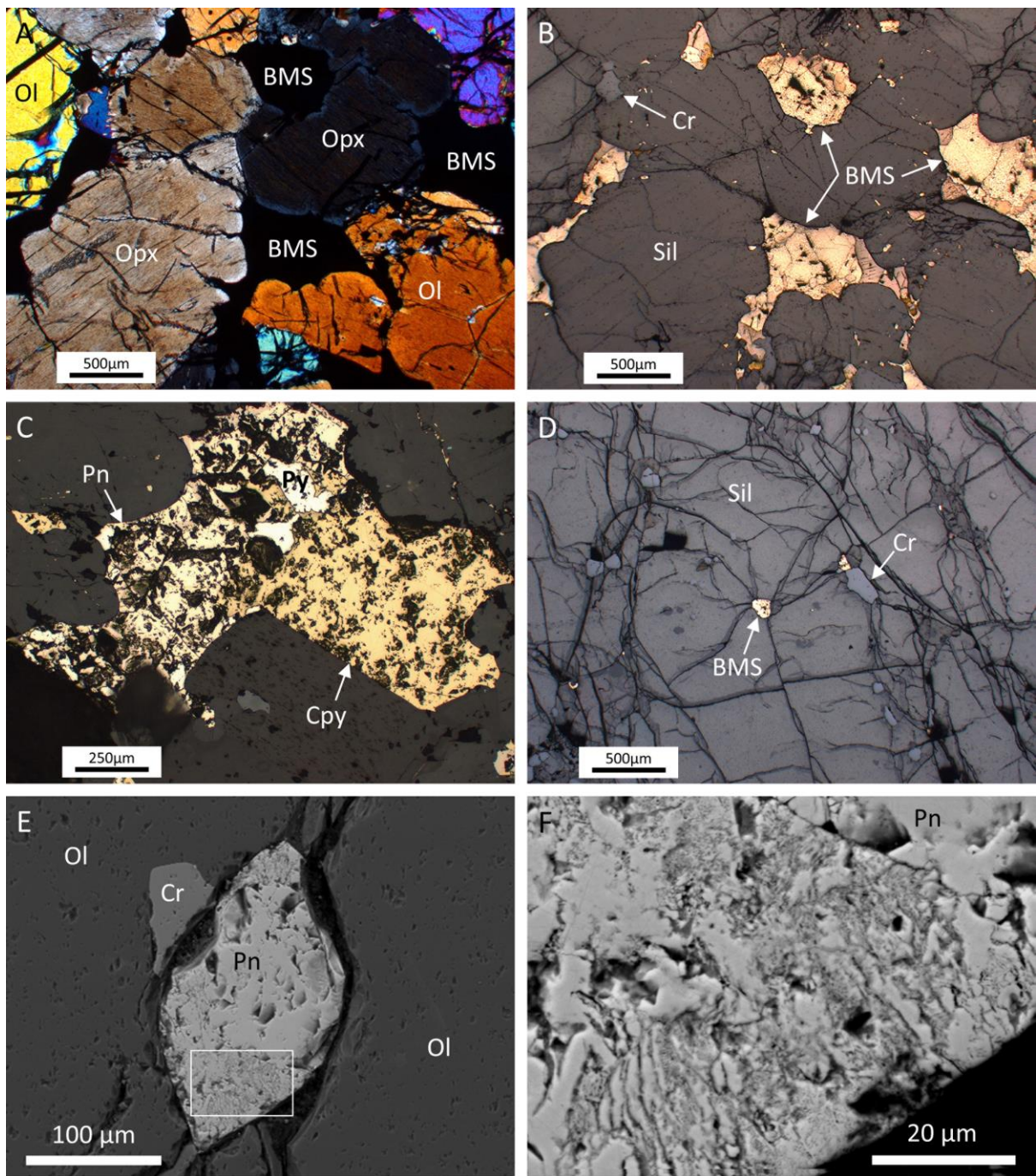
1189

1190

1191

1192

1193



1195

1196

1197

1198

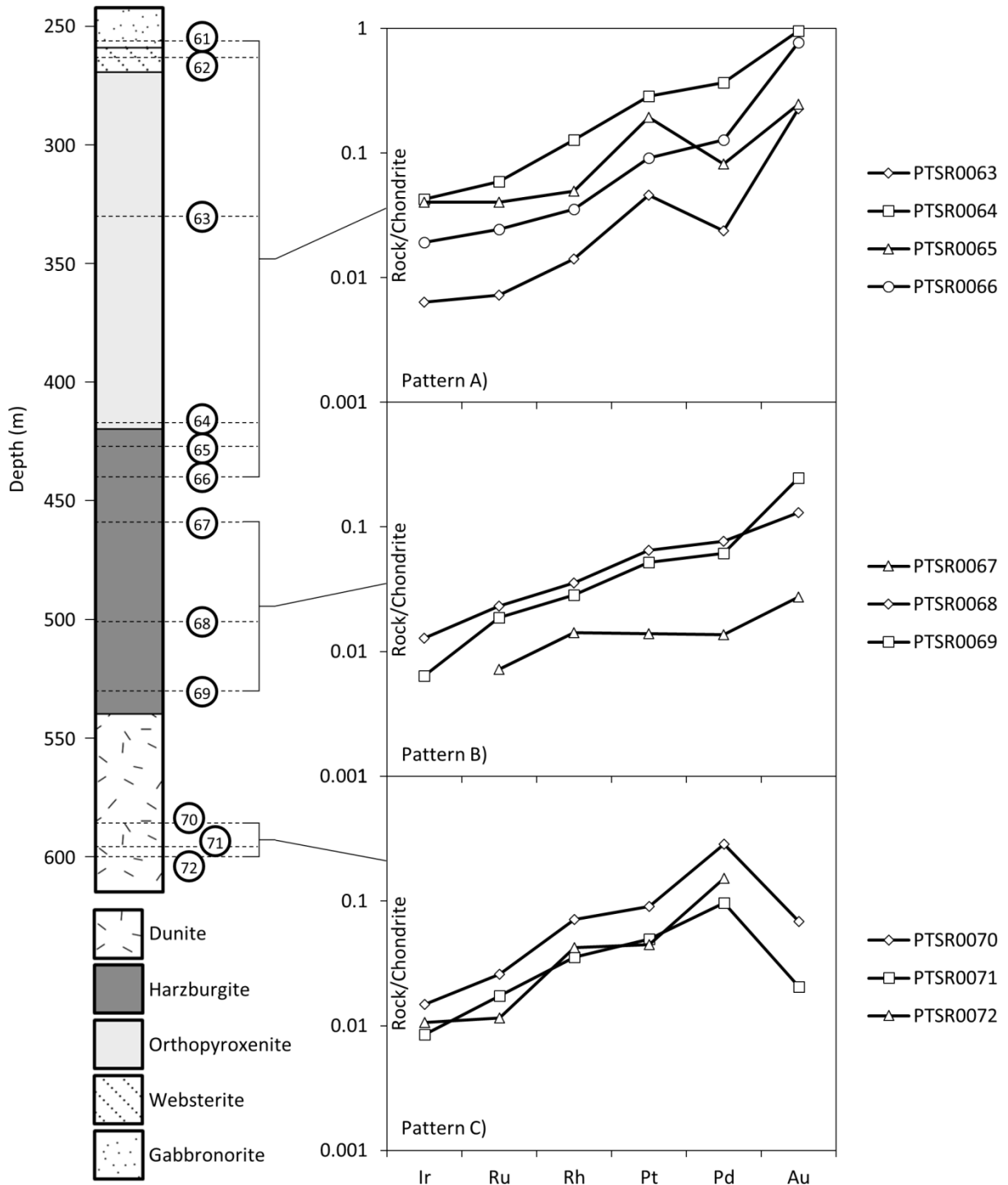
1199

1200

1201

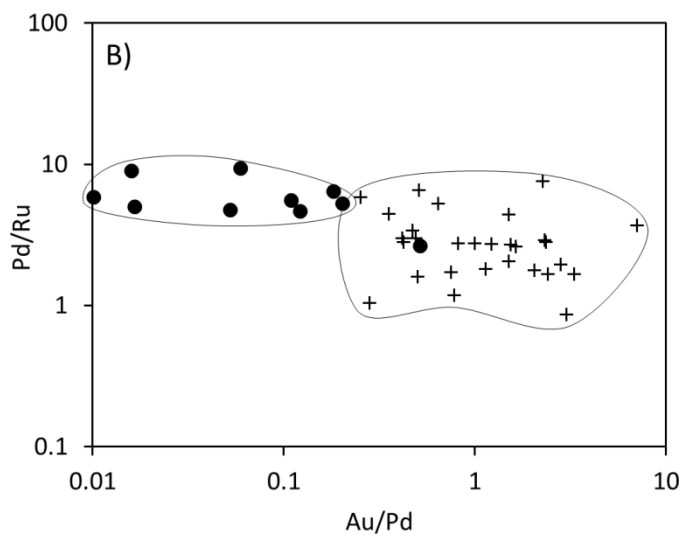
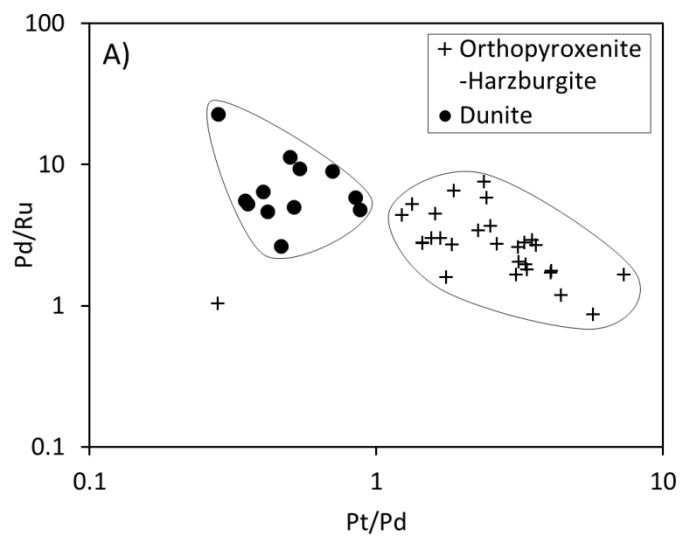
1202

1203 Fig. 5



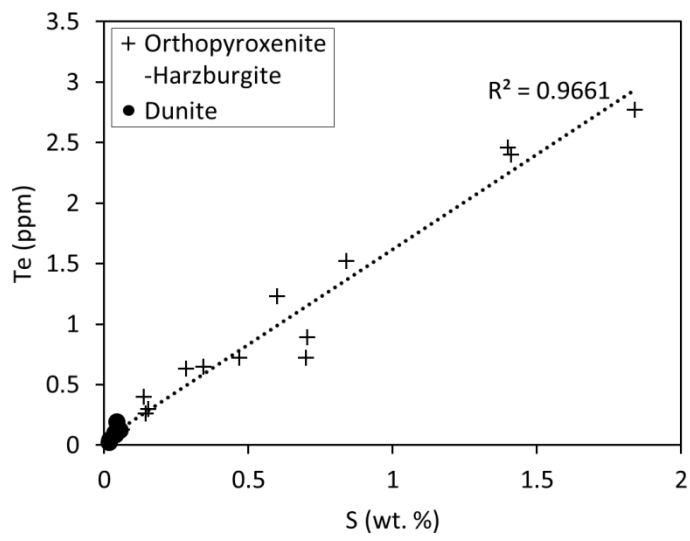
1204  
 1205  
 1206  
 1207  
 1208  
 1209

1210 Fig. 6



1211  
1212  
1213  
1214  
1215  
1216  
1217  
1218  
1219  
1220  
1221  
1222

1223 Fig. 7



1224

1225

1226

1227

1228

1229

1230

1231

1232

1233

1234

1235

1236

1237

1238

1239

1240

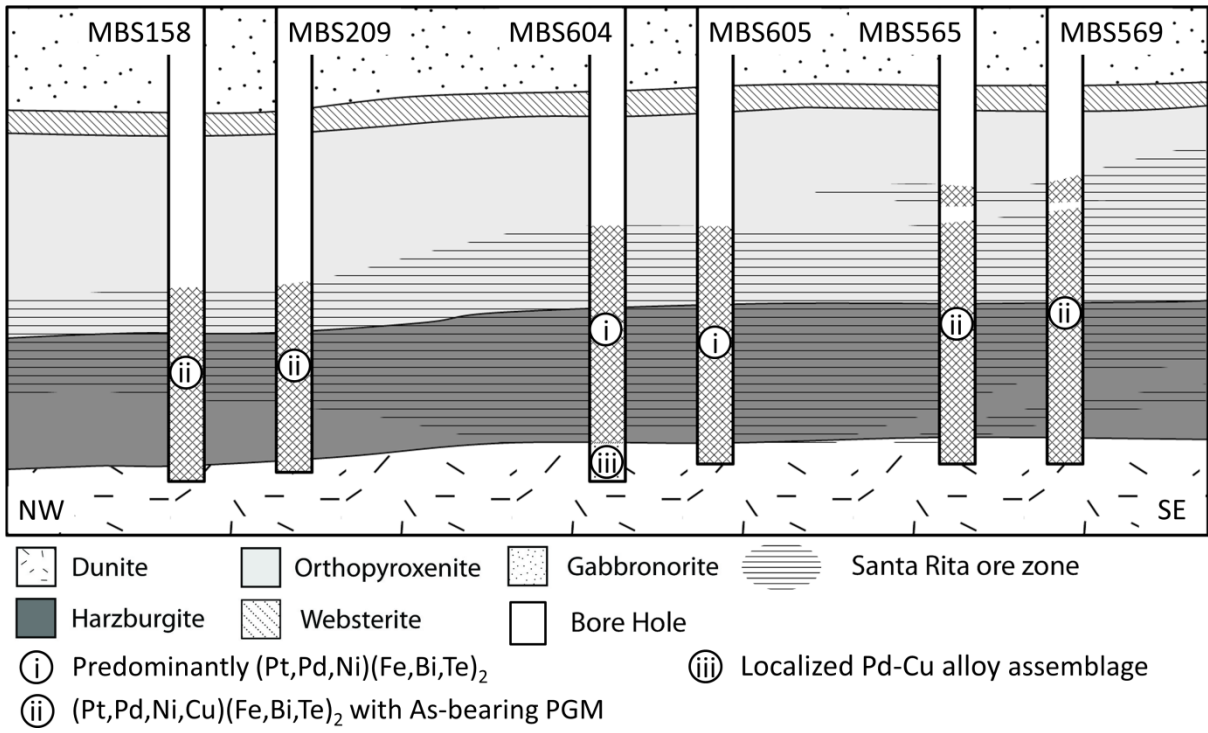
1241

1242

1243

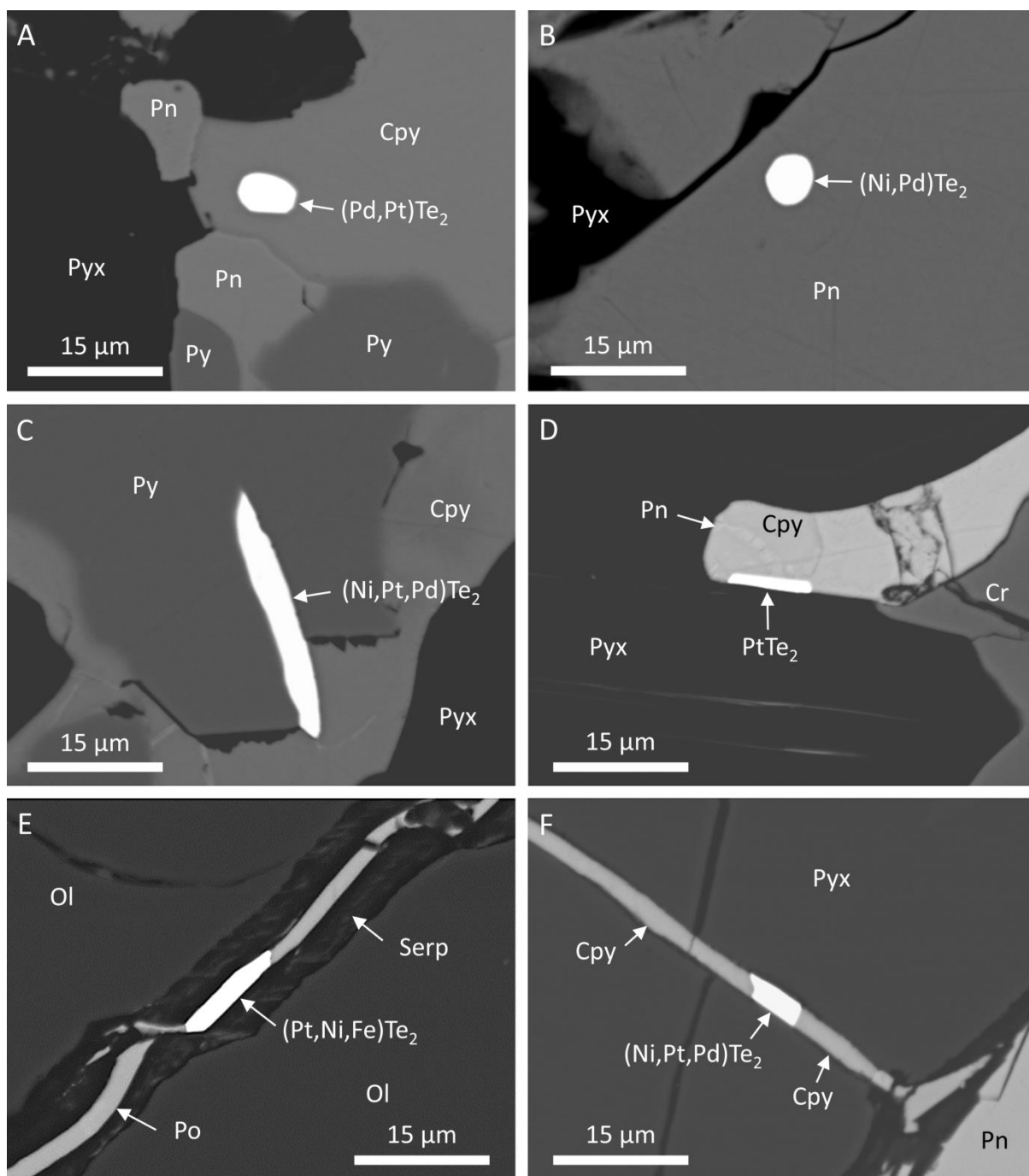
1244

1245 Fig. 8

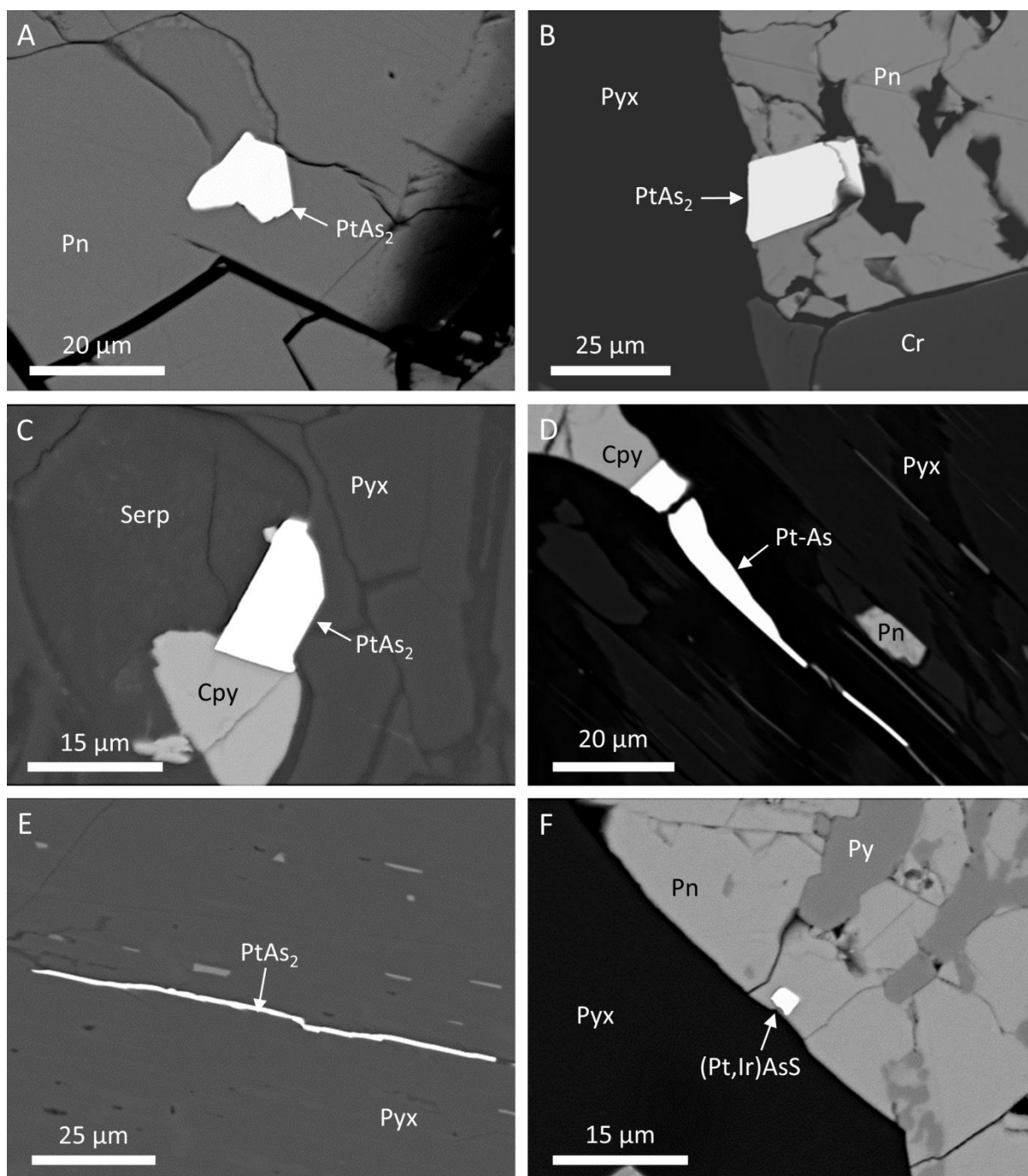


1246  
 1247  
 1248  
 1249  
 1250  
 1251  
 1252  
 1253  
 1254  
 1255  
 1256  
 1257  
 1258  
 1259  
 1260  
 1261  
 1262  
 1263

1264 Fig. 9

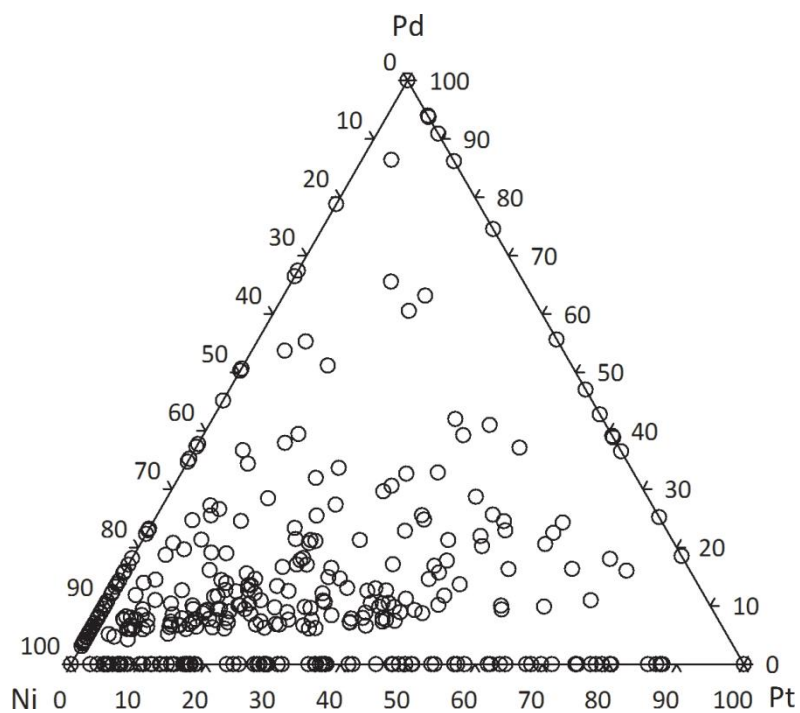


1265  
1266  
1267  
1268  
1269  
1270  
1271  
1272



1274  
1275  
1276  
1277  
1278  
1279  
1280  
1281

1282 Fig. 11



1283 Ni 0 10 20 30 40 50 60 70 80 90 100 Pt

1284

1285

1286

1287

1288

1289

1290

1291

1292

1293

1294

1295

1296

1297

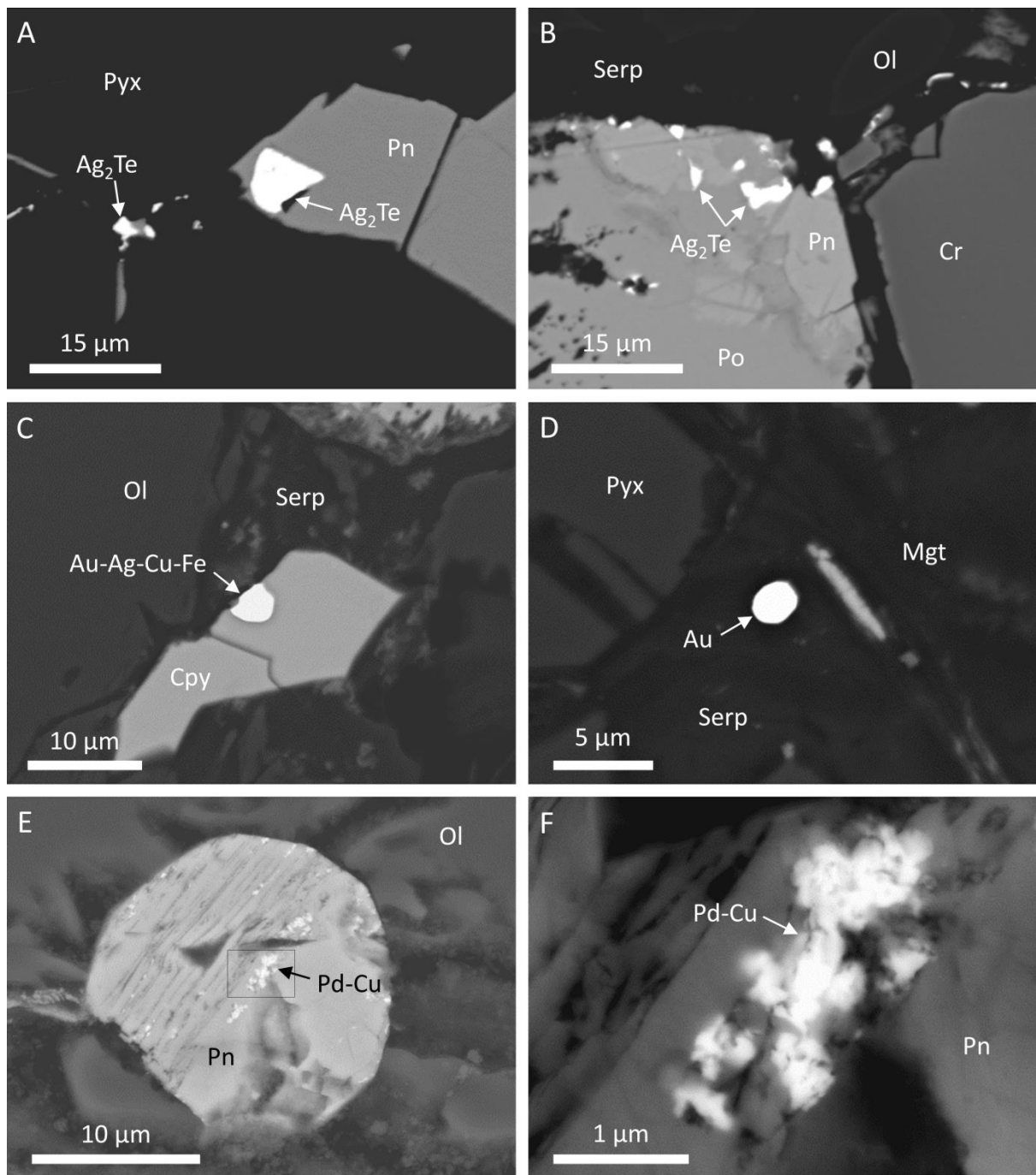
1298

1299

1300

1301

1302 Fig. 12



1303

1304

1305

1306

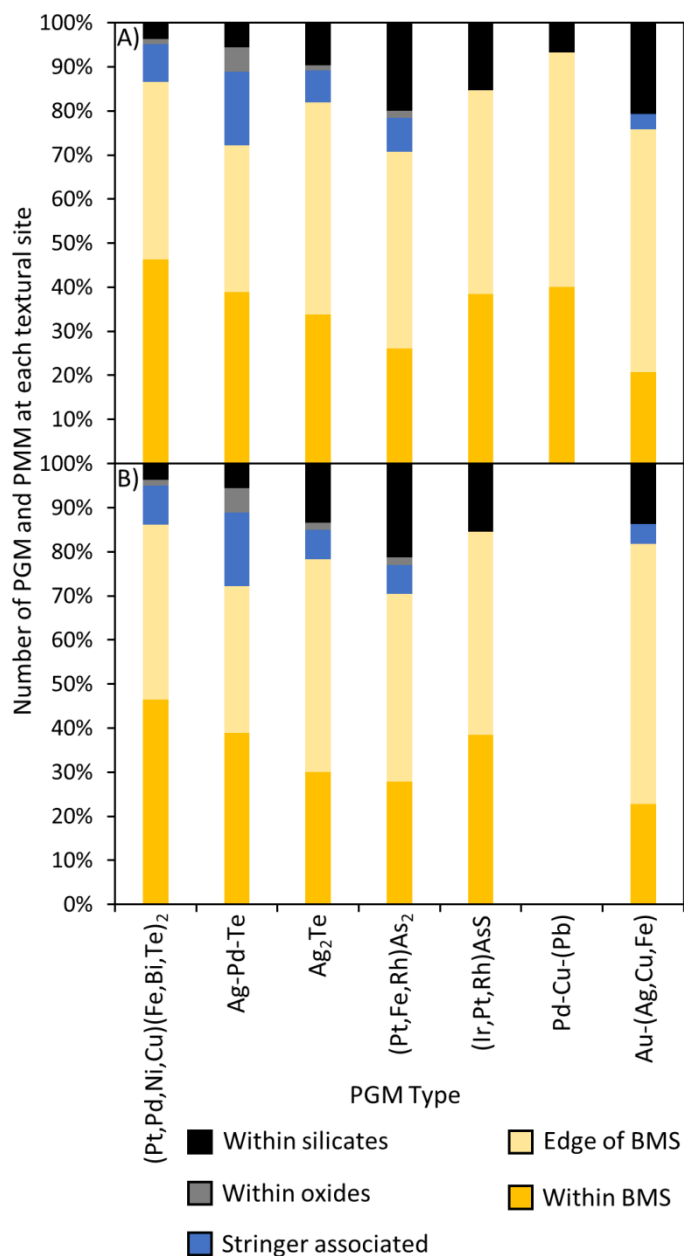
1307

1308

1309

1310

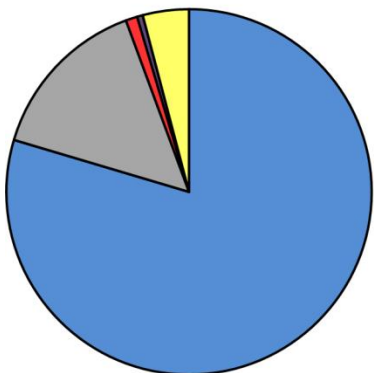
1311 Fig. 13



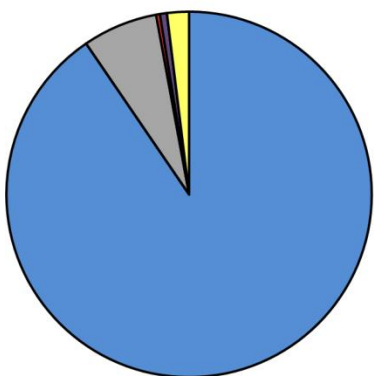
1312  
 1313  
 1314  
 1315  
 1316  
 1317  
 1318  
 1319  
 1320  
 1321

1322 Fig. 14

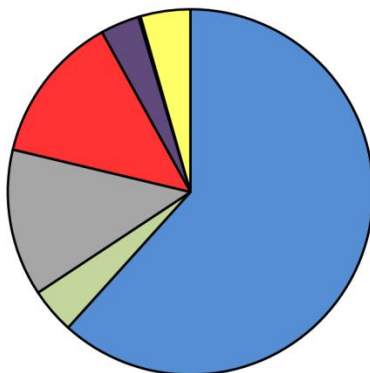
A) Central zone PGM and PMM by number



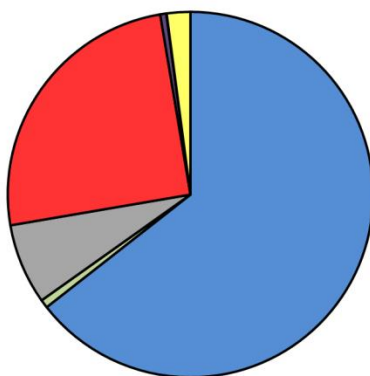
B) Central zone PGM and PMM by area



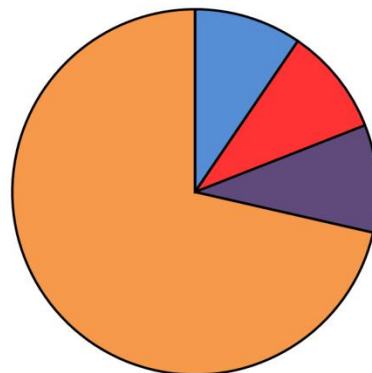
C) Northern and southern zone PGM and PMM by number



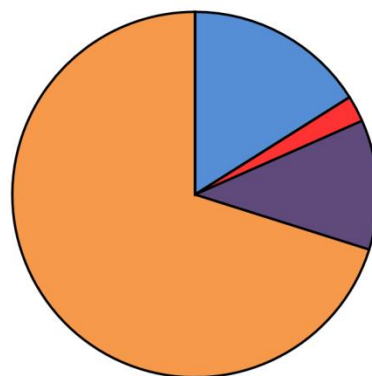
D) Northern and southern zone PGM and PMM by area



E) Pd-Cu alloy assemblage PGM and PMM by number



F) Pd-Cu alloy assemblage PGM and PMM by area



1323

1324

1325

1326

1327

1328

1329

1330

1331

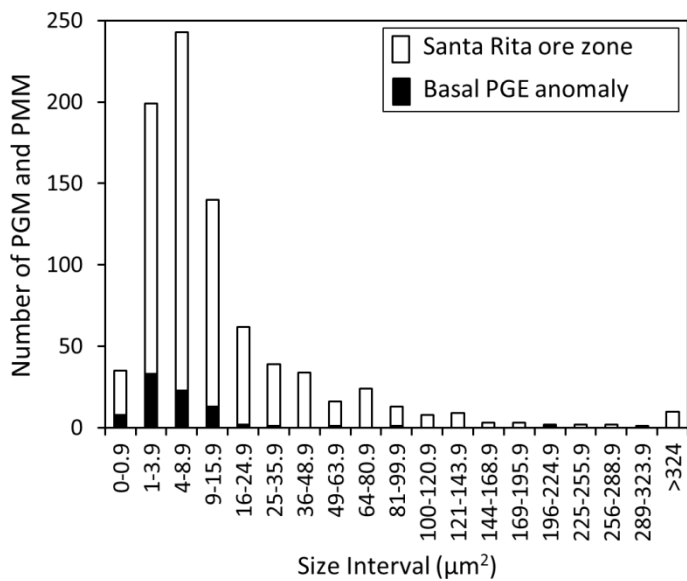
1332

1333

1334

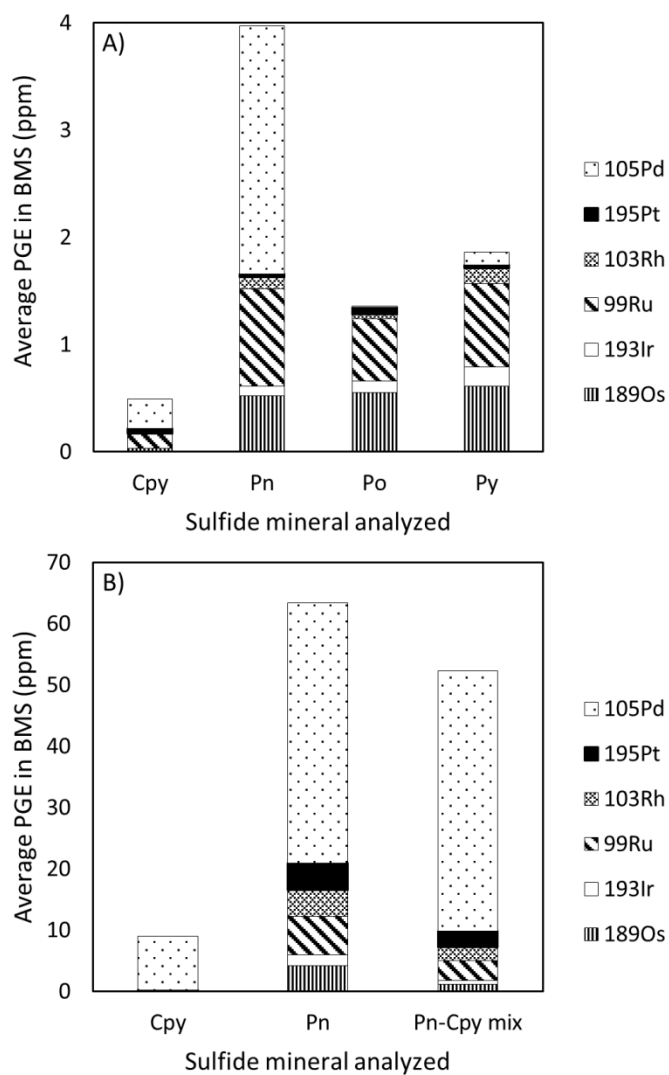
1335

1336 Fig. 15



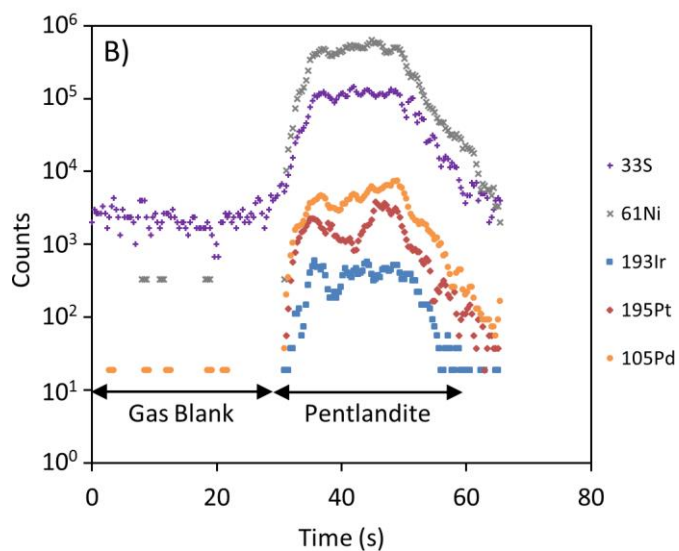
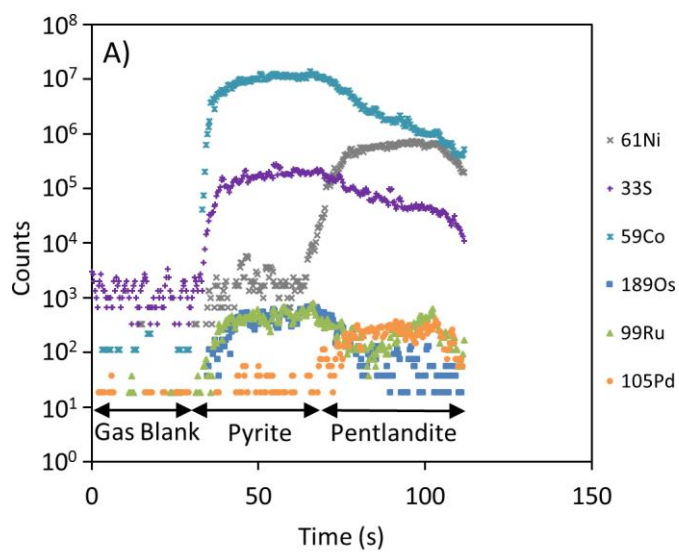
1337  
1338  
1339  
1340  
1341  
1342  
1343  
1344  
1345  
1346  
1347  
1348  
1349  
1350  
1351  
1352  
1353  
1354  
1355  
1356  
1357

1358 Fig. 16



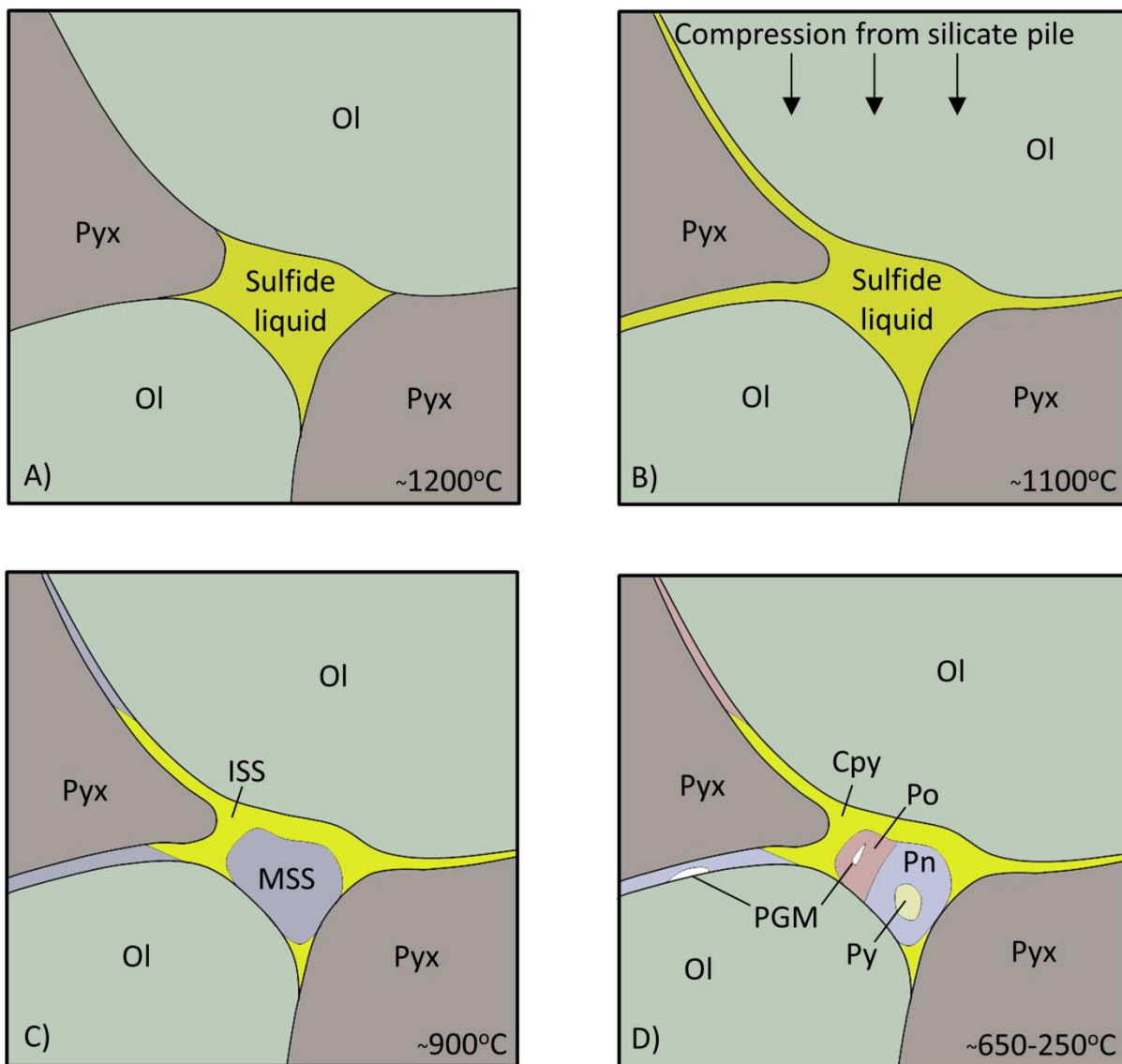
1359  
 1360  
 1361  
 1362  
 1363  
 1364  
 1365  
 1366  
 1367  
 1368  
 1369  
 1370  
 1371

1372 Fig. 17



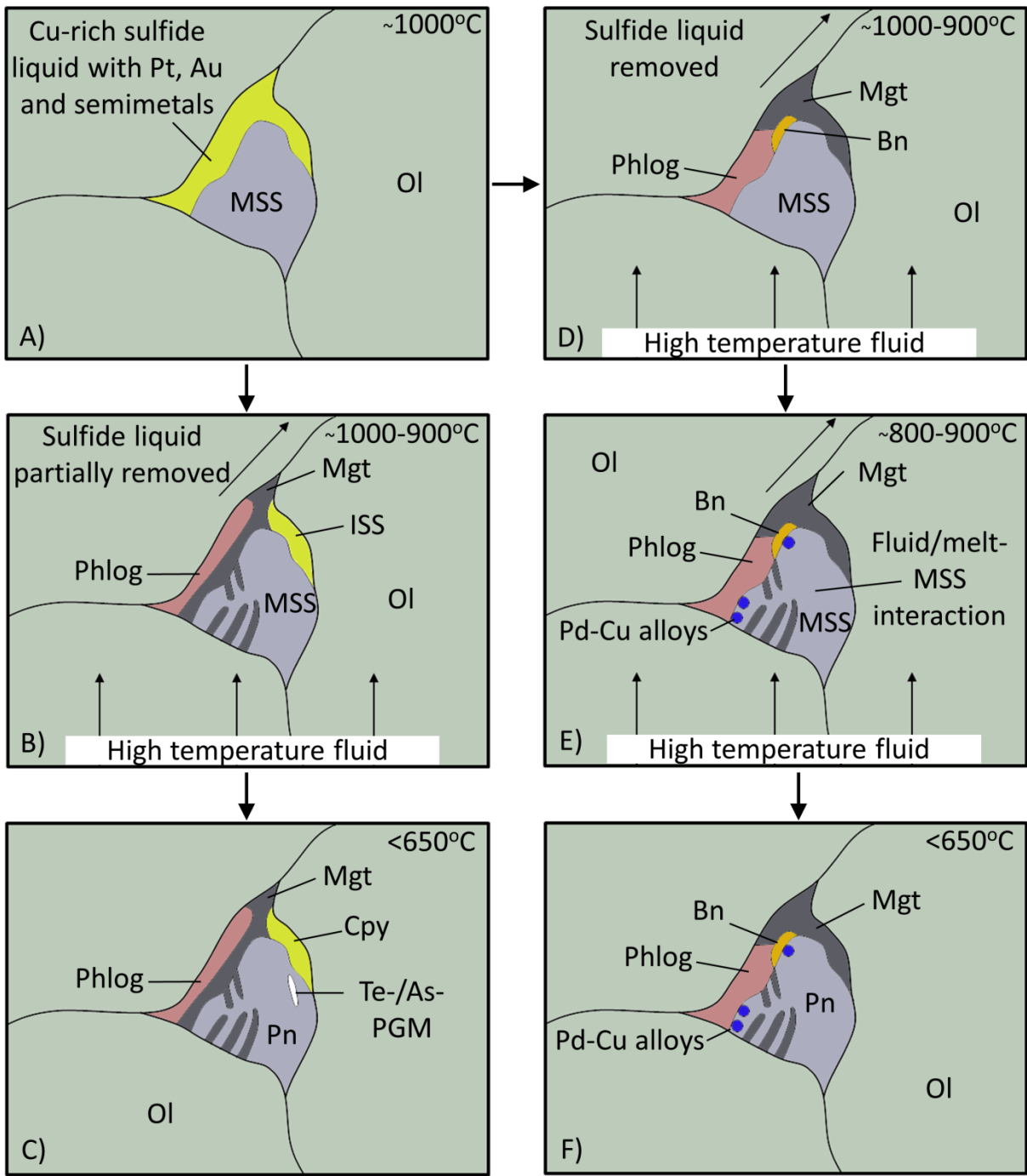
1373  
1374  
1375  
1376  
1377  
1378  
1379  
1380  
1381  
1382  
1383  
1384

1385 Fig. 18



1386  
1387  
1388  
1389  
1390  
1391  
1392  
1393  
1394  
1395  
1396

1397 Fig. 19



1398